THE ASTROPHYSICAL JOURNAL, 468:797–818, 1996 September 10

COLLISIONS OF MAIN-SEQUENCE STARS AND THE FORMATION OF BLUE STRAGGLERS IN GLOBULAR CLUSTERS

JAMES C. LOMBARDI, JR.,[1,2] FREDERIC A. RASIO,[3,4] AND STUART L. SHAPIRO[5]
Received 1995 October 10; accepted 1996 April 4

ABSTRACT

We report the results of new SPH calculations of parabolic collisions between two main-sequence stars in a globular cluster. Such collisions are directly relevant to the formation of blue stragglers. In particular, we consider parent stars of mass $M/M_{TO} = 0.2$, 0.5, 0.75, and 1, where M_{TO} is the cluster turnoff mass (typically about 0.8 $M_\odot$). The parent star models are more realistic, and the numerical resolution of the hydrodynamics more detailed, than in previous studies. We focus on the hydrodynamic mixing of helium and hydrogen, which plays a crucial role in establishing the color, luminosity, and lifetime of collisional blue stragglers. In all cases we find negligible hydrodynamic mixing of helium into the outer envelope of the merger remnant. The amount of hydrogen carried into the core of the merger remnant depends strongly on the entropy profiles of the colliding stars. For stars with nearly equal masses (and hence entropy profiles), the composition profile of the remnant closely resembles that of the parents. If the parent stars were close to turnoff, very little hydrogen is present at the center of the merger remnant and the main-sequence lifetime of the blue straggler could be short. In contrast, during a collision between stars with sufficiently different masses (mass ratio $q \lesssim 0.5$), the hydrogen-rich material originally in the smaller star maintains, on average, a lower specific entropy than that of the more massive star and therefore settles preferentially in the core of the merger remnant. Through this process, moderately massive blue stragglers (with masses $M_{TO} \lesssim M_{BS} \lesssim 1.5M_{TO}$) can obtain a significant supply of fresh hydrogen fuel, thereby extending their main-sequence lifetime. We conclude, in contrast to what has often been assumed, that blue stragglers formed by direct stellar collisions do not necessarily have initially homogeneous composition profiles. However, we also demonstrate that the final merged configurations, although close to hydrostatic equilibrium, are typically far from thermal equilibrium. Therefore, it is possible that convective, semiconvective, or rotationally induced mixing could occur on a thermal timescale, as the merger remnant recontracts to the main sequence.

Subject headings: blue stragglers — hydrodynamics — stars: evolution — stars: interiors — stars: rotation

1. INTRODUCTION AND MOTIVATION

Blue stragglers are stars that appear along an extension of the main sequence (hereafter MS), beyond the turnoff point in the color-magnitude diagram of a cluster. It is generally believed that they are more massive objects (mass $M_{BS} > M_{TO}$) formed by the merger of two MS stars (each of mass less than M_{TO}). Merging can occur through a direct physical collision, or following the coalescence of the two components of a close binary system (Leonard 1989; Livio 1993; Stryker 1993; Bailyn 1995). Clear evidence for binary coalescence has been found in the form of contact binaries among blue stragglers in the low-density globular clusters NGC 5466 (Mateo et al. 1990) and M71 (Yan & Mateo 1994), as well as in open clusters (Kałużny & Ruciński 1993; Milone & Latham 1994; Jahn, Kałużny, & Ruciński 1995). Hills & Day (1976) were the first to suggest that some blue stragglers must be formed by direct stellar collisions. Recent evidence for such collisions comes from detections by the *Hubble Space Telescope* of large numbers of blue stragglers concentrated in the cores of some of the densest clusters, such as M15 (De Marchi & Paresce 1994; Yanny et al. 1994a) and M30 (Yanny et al. 1994b), and from the apparent lack of binaries in such dense systems (Shara et al. 1995). Collisions can happen directly between two single stars only in the cores of the densest clusters, but even in somewhat lower density clusters they can also happen indirectly, during resonant interactions involving primordial binaries (Leonard 1989; Leonard & Fahlman 1991; Sigurdsson, Davies, & Bolte 1994; Sigurdsson & Phinney 1995; Davies & Benz 1995). Observational evidence for dynamically significant numbers of primordial binaries in globular clusters is now well established (Hut et al. 1992; Côté et al. 1994).

Benz & Hills (1987, hereafter BH) performed the first three-dimensional calculations of direct collisions between two MS stars. An important conclusion of their pioneering study was that grazing collisions lead to nearly complete mixing of the fluid. The mixing of fresh hydrogen fuel into the core of the merger remnant would reset the nuclear clock of the blue straggler, allowing it to remain on the MS for up to $\sim 10^9$ yr after its formation. Even though BH's collisions at small impact parameters reveal only partial mixing, subsequent works generally assumed that all collisional blue stragglers were born nearly homogeneous in composition. Such blue stragglers would start their lives close to the zero-age MS, but with an anomalously high helium abundance coming from the (evolved) parent stars. In contrast, less hydrodynamic mixing would be expected during

[1] Center for Radiophysics and Space Research, Cornell University, Ithaca, NY 14853; lombardi@spacenet.tn.cornell.edu.
[2] Department of Astronomy, Cornell University.
[3] Department of Physics, MIT 6-201, Cambridge, MA 02139; rasio@mit.edu.
[4] Alfred P. Sloan Research Fellow.
[5] Department of Physics, University of Illinois at Urbana-Champaign, 1110 West Green Street, Urbana, IL 61801.

the gentler process of binary coalescence, which could take place on a stellar evolution timescale rather than on a dynamical timescale (Mateo et al. 1990; Bailyn 1992; but see Rasio & Shapiro 1995 and Rasio 1995).

On the basis of these ideas, Bailyn (1992) suggested a way of distinguishing observationally between the two possible formation processes. The helium abundance in the envelope of a blue straggler, which reflects the degree of mixing during its formation process, can affect its observed position in a color-magnitude diagram. Blue stragglers made from collisions would have a higher helium abundance in their outer layers than those made from binary mergers, and this would generally make them appear somewhat brighter and bluer. The analysis was carried out by Bailyn & Pinsonneault (1995), who performed detailed stellar evolution calculations for blue stragglers assuming various initial profiles. To represent the collisional case, they again assumed chemically homogeneous initial profiles with enhanced helium abundances, calculating the total helium mass from the age of the cluster and the masses of the parent stars.

In this paper, we use smoothed particle hydrodynamics (SPH) simulations of stellar collisions to reexamine the question of fluid mixing. We improve on the previous work of BH by adopting more realistic models for MS stars and by performing the numerical calculations with increased spatial resolution. Since SPH is a Lagrangian method, in which particles are used to represent fluid elements, it is ideally suited for the study of hydrodynamic mixing. Indeed, with the assumption that the gas remains fully ionized throughout the dynamical evolution, chemical abundances are passively advected quantities. Therefore, the chemical composition in the final fluid configuration can be determined after the completion of a calculation simply by noting the initial and final positions of all SPH particles and then assigning chemical abundances according to composition profiles of the parent stars.

The colliding stars in our calculations are modeled as polytropes or composite polytropes (Chandrasekhar 1939; Rappaport, Verbunt, & Joss 1983; Ruciński 1988), and we adopt an ideal gas equation of state. The polytropic index n relates the pressure and density profiles in the star according to $P \propto \rho^{1+1/n}$. The adiabatic index $\Gamma_1 = 5/3$ for an ideal gas, with the equation of state being $P = A\rho^{\Gamma_1}$. Here A is a physical parameter related to the local specific entropy s according to $A \propto \exp[(\Gamma_1 - 1)s/k]$, where k is Boltzmann's constant. When $\Gamma_1 \neq 1 + 1/n$ the quantity A, and hence the entropy s, has a nonzero gradient. BH used $n = 1.5$, $\Gamma_1 = 5/3$ polytropic models to represent MS stars. Unfortunately, such models apply only to very low-mass MS stars with large convective envelopes: for Population II MS stars, the effective polytropic index (defined in terms of the degree of central mass concentration) is close to $n = 1.5$ only for a mass $M \lesssim 0.4\, M_\odot$ (see Lai, Rasio, & Shapiro 1994, Table 3). The object formed by a merger of two such low-mass stars would hardly be recognizable as a blue straggler, since it would lie below, or not far above, the MS turnoff point (typically $M_{\rm TO} \approx 0.8\, M_\odot$) in a color-magnitude diagram.

Stars near the MS turnoff point have little mass in their convective envelopes and are much better described by $n = 3$, $\Gamma_1 = 5/3$ polytropes (Eddington's "standard model"; see, e.g., Clayton 1983). The mass distribution of such stars is much more centrally concentrated than in $n = 1.5$ polytropes, which has important consequences for the hydrodynamics of collisions. Population II MS stars with masses in the intermediate range $0.4\, M_\odot \lesssim M \lesssim 0.8\, M_\odot$ can be modeled by composite polytropes with a polytropic index of $n = 3$ for the radiative core and $n = 1.5$ for the convective envelope.

Stars close to the MS turnoff point in a cluster are the most relevant to consider for stellar collision calculations for two reasons. First, as the cluster evolves via two-body relaxation, the more massive MS stars will tend to concentrate in the dense cluster core, where the collision rate is highest (see, e.g., Spitzer 1987). Second, collision rates can be increased dramatically by the presence of a significant fraction of primordial binaries in the cluster, and the more massive MS stars will preferentially tend to be exchanged into such a binary, or collide with another star, following a dynamical interaction between two binaries or between a binary and a single star (Sigurdsson & Phinney 1995; Bacon, Sigurdsson, & Davies 1996).

Lai et al. (1993) have calculated collisions between MS stars modeled by $n = 3$, $\Gamma_1 = 5/3$ polytropes, but they focused on high-velocity (hyperbolic) collisions more relevant to galactic nuclei than to globular clusters. The velocity dispersion of globular cluster stars is typically ~ 10 km s^{-1}, which is much smaller than the escape velocity from the stellar surface [for example, a MS star of mass $M = 0.8\, M_\odot$ and radius $R = R_\odot$ has an escape velocity $(2GM/R)^{1/2} = 552$ km s^{-1}]. For this reason, we consider only parabolic collisions in this paper, i.e., all initial trajectories are assumed to have zero orbital energy.

Our paper is organized as follows. In § 2 we describe our implementation of the SPH method and the numerical setup of our calculations. In § 3 we present the models used for the parent MS stars, detailing their assumed structure and chemical composition profiles. We also describe the initial ($t = 0$) configuration of the trajectory. Our results are presented in § 4. After describing the results for two typical collisions in detail, we then characterize the rotation states and the final profiles of all our merger remnants. We also present a general method, which does not depend on our particular choice of initial chemical composition profiles, for calculating the final profile of any passively advected quantity in the merger remnant. We conclude our results with an analysis of the numerical accuracy of our simulations. Finally, in § 5 we discuss the astrophysical implications of our results as well as directions for future work.

2. NUMERICAL METHOD AND CONVENTIONS

2.1. *The SPH Code*

Our numerical calculations are done using the smoothed particle hydrodynamics (SPH) method (see Monaghan 1992 for a recent review). We use a modified version of the code developed by Rasio (1991) specifically for the study of stellar interactions (see Rasio & Shapiro 1995, and references therein). In this subsection, we briefly describe our particular implementation of the SPH scheme.

Associated with each SPH particle i is its position $\boldsymbol{r}_i$, velocity $\boldsymbol{v}_i$, mass m_i, and a purely numerical "smoothing length" h_i specifying the local spatial resolution. An estimate of the fluid density at $\boldsymbol{r}_i$ is calculated from the masses, positions, and smoothing lengths of neighboring particles as a local weighted average:

$$\rho_i = \sum_j m_j W_{ij}\,, \tag{1}$$

where the symmetric weights $W_{ij} = W_{ji}$ are calculated from the method of Hernquist & Katz (1989), as

$$W_{ij} = \tfrac{1}{2}[W(|\boldsymbol{r}_i - \boldsymbol{r}_j|, h_i) + W(|\boldsymbol{r}_i - \boldsymbol{r}_j|, h_j)] . \quad (2)$$

Here $W(r, h)$ is an interpolation kernel, for which we use the second-order accurate form of Monaghan & Lattanzio (1985):

$$W(r, h) = \frac{1}{\pi h^3} \begin{cases} 1 - \frac{3}{2}\left(\frac{r}{h}\right)^2 + \frac{3}{4}\left(\frac{r}{h}\right)^3 , & 0 \le \frac{r}{h} < 1 ; \\ \frac{1}{4}\left[2 - \left(\frac{r}{h}\right)\right]^3 , & 1 \le \frac{r}{h} < 2 ; \\ 0 , & \frac{r}{h} \ge 2 . \end{cases} \quad (3)$$

In addition to passively advected scalar quantities (such as the helium mass fraction Y_i), each particle i also carries the local entropy variable A_i. The specific entropy s_i at $\boldsymbol{r}_i$ is related to A_i by

$$s_i - s_o = \frac{k}{\Gamma_1 - 1} \ln A_i , \quad (4)$$

where k is Boltzmann's constant and s_o is a constant. Neglecting radiation pressure, the pressure at $\boldsymbol{r}_i$ is estimated as

$$p_i = A_i \rho_i^{\Gamma_1} , \quad (5)$$

where the adiabatic index $\Gamma_1 = 5/3$ is the ratio of specific heats for a fully ionized ideal gas. As a self-consistency test of our ideal gas approximation, we have checked that the vast majority of particles have p_i remaining much larger than the radiation pressure $\frac{1}{3}aT_i^4$, where a is the radiation constant and T_i is the local temperature, throughout the dynamical evolution.

An SPH code must solve the equations of motion of a large number N of Lagrangian fluid particles. Particle positions are updated according to

$$\dot{\boldsymbol{r}}_i = \boldsymbol{v}_i , \quad (6)$$

while the velocity of particle i is updated according to

$$m_i \dot{\boldsymbol{v}}_i = \boldsymbol{F}_i^{(\mathrm{Grav})} + \boldsymbol{F}_i^{(\mathrm{SPH})} . \quad (7)$$

Here the gravitational force $\boldsymbol{F}_i^{(\mathrm{Grav})}$ is calculated by a particle-mesh convolution algorithm (Hockney & Eastwood 1988; Wells et al. 1990) based on fast Fourier transforms (FFT) on a 256^3 grid and

$$\boldsymbol{F}_i^{(\mathrm{SPH})} = -\sum_j m_i m_j \left[\left(\frac{p_i}{\rho_i^2} + \frac{p_j}{\rho_j^2}\right) + \Pi_{ij}\right] \nabla_i W_{ij} . \quad (8)$$

The Π_{ij} term accounts for the artificial viscosity described below, while the rest of equation (8) represents one of many possible SPH estimators for the local pressure-gradient force $-m_i(\nabla p/\rho)_i$ (see, e.g., Monaghan 1985).

For the artificial viscosity, a symmetrized version of the form proposed by Monaghan & Lattanzio (1985) is adopted:

$$\Pi_{ij} = \frac{-\alpha \mu_{ij} c_{ij} + \beta \mu_{ij}^2}{\rho_{ij}} , \quad (9)$$

where α and β are constant parameters, $c_{ij} = (c_i + c_j)/2$, and

$$\mu_{ij} = \begin{cases} \dfrac{(\boldsymbol{v}_i - \boldsymbol{v}_j)\cdot(\boldsymbol{r}_i - \boldsymbol{r}_j)}{h_{ij}(|\boldsymbol{r}_i - \boldsymbol{r}_j|^2/h_{ij}^2 + \eta^2)} , & \text{when } (\boldsymbol{v}_i - \boldsymbol{v}_j)\cdot(\boldsymbol{r}_i - \boldsymbol{r}_j) < 0 ; \\ 0 , & \text{when } (\boldsymbol{v}_i - \boldsymbol{v}_j)\cdot(\boldsymbol{r}_i - \boldsymbol{r}_j) \ge 0 , \end{cases} \quad (10)$$

with $h_{ij} = (h_i + h_j)/2$. We have used $\alpha = 1$, $\beta = 2$ and $\eta^2 = 0.01$, which provides a good description of shocks (Monaghan 1989; Hernquist & Katz 1989).

To complete the evolution equations of the fluid, A_i is evolved according to a discretized version of the first law of thermodynamics:

$$\frac{dA_i}{dt} = \frac{\gamma - 1}{2\rho_i^{\gamma - 1}} \sum_j m_j \Pi_{ij} (\boldsymbol{v}_i - \boldsymbol{v}_j)\cdot\nabla_i W_{ij} . \quad (11)$$

Equation (11) has the advantage that the total entropy is strictly conserved in the absence of shocks (i.e., when $\Pi_{ij} = 0$), and the disadvantage that the total energy is only approximately conserved (Rasio 1991; Hernquist 1993). Both total energy and angular momentum conservation are monitored throughout the integrations as a measure of numerical accuracy, and these quantities are conserved typically at the percent level.

The dynamical equations are integrated using a second-order explicit leap-frog scheme. We calculate the time step as $\Delta t = C_N \,\mathrm{Min}\,(\Delta t_1, \Delta t_2)$, where $\Delta t_1 = \mathrm{Min}_i\,(h_i/\dot{\boldsymbol{v}}_i)^{1/2}$, $\Delta t_2 = \mathrm{Min}_i\,[h_i/(c_i^2 + v_i^2)^{1/2}]$ and the Courant number $C_N = 0.8$. Other details of our implementation, as well as a number of test-bed calculations using our SPH code are presented in Lombardi, Rasio, & Shapiro (1996).

Twenty of the 23 calculations reported here employ $N = 3 \times 10^4$ equal-mass particles, while the remaining three calculations (cases U, V, and W below) use $N = 1.8 \times 10^4$ equal-mass particles. Unequal-mass SPH particles, sometimes used to allow for higher resolution in low-density regions, tend to settle spuriously to preferred regions in the gravitational potential because of numerical discreteness effects. Therefore, even though equal-mass particles can lead to poor resolution in low-density stellar envelopes, they are still the appropriate choice for studies of fluid mixing. In all of our simulations, time-dependent, individual particle smoothing lengths h_i ensure that each particle interacts with a constant number of neighbors $N_N \approx 64$. The numerical integration of the SPH equations typically takes about 2 CPU hours per time unit (eq. [12] below) on an IBM SP-2 supercomputer.

2.2. *Choice of Units*

Throughout this paper, numerical results are given in units where $G = M_{\mathrm{TO}} = R_{\mathrm{TO}} = 1$, where G is Newton's gravitational constant, and M_{TO} and R_{TO} are the mass and radius of a terminal-age MS (TAMS) star at the cluster turnoff point. The units of time, velocity, and density are then

$$t_u = \left(\frac{R_{\mathrm{TO}}^3}{GM_{\mathrm{TO}}}\right)^{1/2} = 1782\ \mathrm{s}\left(\frac{M_{\mathrm{TO}}}{0.8\ M_\odot}\right)^{-1/2}\left(\frac{R_{\mathrm{TO}}}{R_\odot}\right)^{3/2} , \quad (12)$$

$$v_u = \left(\frac{GM_{\mathrm{TO}}}{R_{\mathrm{TO}}}\right)^{1/2} = 391\ \mathrm{km\ s^{-1}}\left(\frac{M_{\mathrm{TO}}}{0.8\ M_\odot}\right)^{1/2}\left(\frac{R_{\mathrm{TO}}}{R_\odot}\right)^{-1/2} , \quad (13)$$

$$\rho_u = \frac{M_{\rm TO}}{R_{\rm TO}^3} = 4.72 \text{ g cm}^{-3} \left(\frac{M_{\rm TO}}{0.8\ M_\odot}\right)\left(\frac{R_{\rm TO}}{R_\odot}\right)^{-3}. \quad (14)$$

Furthermore, the units of temperature and specific entropy are chosen to be

$$T_u = \frac{GM_{\rm TO} m_{\rm H}}{kR_{\rm TO}} = 1.85 \times 10^7 \text{ K}\left(\frac{M_{\rm TO}}{0.8\ M_\odot}\right)\left(\frac{R_{\rm TO}}{R_\odot}\right)^{-1}, \quad (15)$$

$$s_u = \frac{k}{M_{\rm TO}} = 8.68 \times 10^{-50} \text{ erg K}^{-1} \text{ g}^{-1}\left(\frac{M_{\rm TO}}{0.8\ M_\odot}\right)^{-1}, \quad (16)$$

where $m_{\rm H}$ is the mass of hydrogen and k is Boltzmann's constant.

2.3. *Determination of the Bound Mass and Termination of the Calculation*

The iterative procedure used to determine the total amount of gravitationally bound mass M of a merger remnant is the same as in Rasio (1991): namely, to be considered bound, a particle must have negative specific enthalpy with respect to the bound fluid's center of mass. During all of the stellar collisions we considered, only a small fraction (typically a few percent) of the ejected mass becomes gravitationally unbound. Some SPH particles, although bound, are ejected so far away from the system's center of mass that it would take many dynamical timescales for them to rain back onto the central remnant and settle into equilibrium. Rather than wait for these particles (which would allow for more spurious dissipation and mixing; see §§ 4.2 and 4.5), we terminate the calculation once we are confident that at least the inner 95% of the mass has settled into equilibrium. We confirm this by two stability tests. First, we check that the specific entropy s increases from the center to the surface of the merger remnant, a sufficient (and necessary for nonrotating stars) condition for convective stability (see the discussion surrounding eq. [18]). For rotating merger remnants we also check another dynamical stability criteria, namely that the specific angular momentum increases from the poles to the equator along surfaces of constant entropy (Tassoul 1978).

3. INITIAL DATA

We consider parent MS stars of masses $M = 0.2, 0.5, 0.75$, and $1M_{\rm TO}$. Table 1 gives the stellar radius R that we adopt, as well as the radii enclosing mass fractions 0.9 and 0.95, for each of these parent stars. Note the central concentration of mass in the $M = M_{\rm TO}$, $R = R_{\rm TO}$ star: 90% of its mass lies within a sphere of radius $0.503R_{\rm TO}$, so that 10% of the (equal-mass) SPH particles are used to model the outer 87% of the volume. Whereas the numerical resolution is consequently somewhat lower in the envelope of such a star, we do note that all of our parent models have more than 1500 particles with $r/R > 0.5$.

TABLE 1

PARENT STAR CHARACTERISTICS

M	R	$r(0.9M)$	$r(0.95M)$	$M_{\rm He}/M$
0.2.....	0.16	0.124	0.133	0.240
0.5.....	0.37	0.286	0.307	0.250
0.75.....	0.56	0.422	0.457	0.283
1.....	1	0.503	0.573	0.411

The $M = 0.2$ and $0.5M_{\rm TO}$ stars are modeled as $n = 1.5$ polytropes, whereas the $M = M_{\rm TO}$ stars have the structure of $n = 3$ polytropes. The $0.75M_{\rm TO}$ stars are modeled as composite polytropes consisting of a radiative core of index $n = 3$ and a convective envelope of index $n = 1.5$, with the interface being located at a radius $0.29R_{\rm TO}$. This interface radius, as well as the stellar radii for all the parent stars, is obtained from the stellar evolution calculations by D'Antona (1987) for Population II stars of primordial helium abundance $Y = 0.23$ and metallicity $Z = 0.0001$. The results were interpolated assuming $M_{\rm TO} = 0.8\ M_\odot$ to an age $t = 15$ Gyr.

The top frame of Figure 1 shows the resulting specific entropy profiles as given by one-dimensional numerical integrations. The convective regions have constant specific entropy. Note that the specific entropy in the $M = 0.2$ and $0.5M_{\rm TO}$ stars is everywhere smaller than the minimum specific entropy in the two more massive stars; this fact plays a central role in understanding the dynamics of the merger involving either an $M = 0.2$ or $0.5M_{\rm TO}$ star with a more massive star. For comparison, the bottom frame of Figure 1 shows the three-dimensional SPH entropy profile for our $M = M_{\rm TO}$ parent star with $N = 1.5 \times 10^4$ particles, superimposed on the one-dimensional result. The central concentration of the $M = M_{\rm TO}$ star, along with the use of equal-mass SPH particles, leads to the relatively small number of particles in the outer layers; nevertheless, the agreement between the SPH and one-dimensional profiles remains excellent throughout the star. In all of our other parent models, the outer layers have a larger number density of SPH particles and hence a better resolution.

We have used the stellar evolution code developed by Sienkiewicz and collaborators (see Sienkiewicz, Bahcall, &

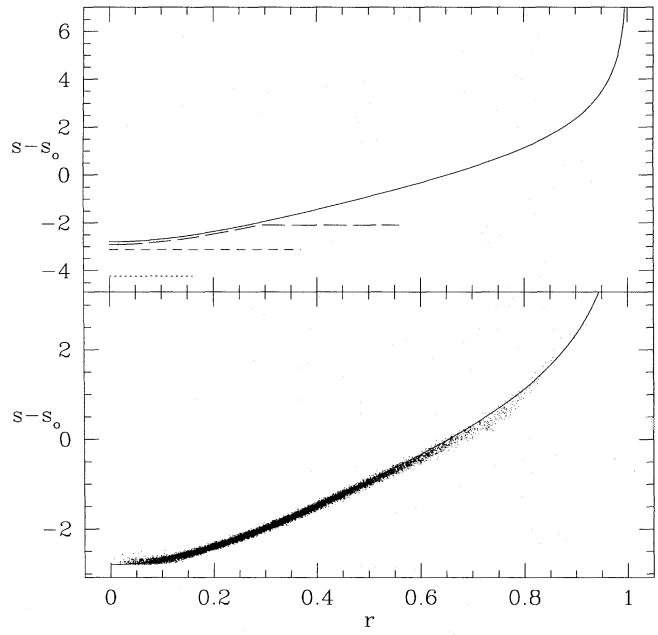

FIG. 1.—Specific entropy s (relative to the constant s_o) as a function of radius r for the parent stars used in our collision calculations. The dotted, short-dashed, long-dashed, and solid curves in the top frame correspond to the results of a one-dimensional integration for our parent stars of mass $M = 0.2$, 0.5, 0.75, and $1M_{\rm TO}$, respectively, where $M_{\rm TO} = 0.8\ M_\odot$ is the mass of a turnoff star. The bottom frame shows the SPH particle values of the entropy for our $M = M_{\rm TO}$ star with $N = 1.5 \times 10^4$ particles, superimposed on the one-dimensional result. Units are defined in § 2.2.

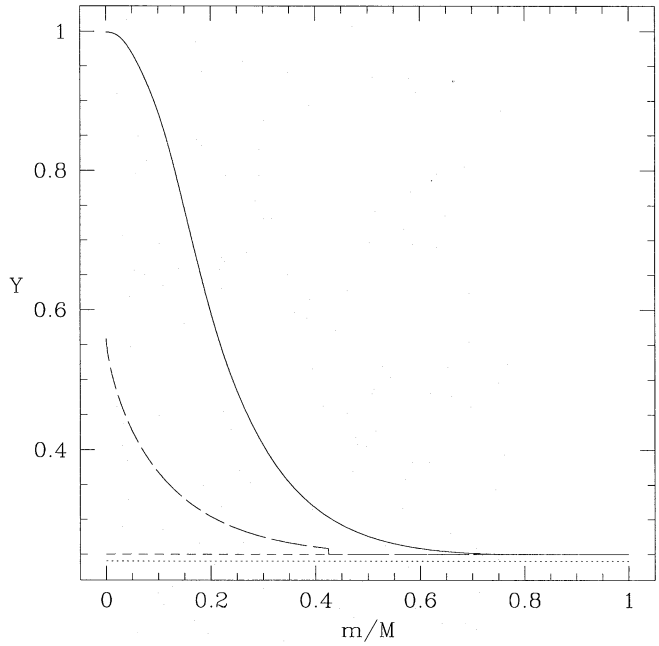

FIG. 2.—Fractional helium abundance Y as a function of interior mass fraction m/M for the parent stars whose entropy profiles are shown in Fig. 1. As in Fig. 1, the dotted, short-dashed, long-dashed, and solid curves correspond to parent stars of mass $M = 0.2$, 0.5, 0.75, and $1M_{\rm TO}$, respectively.

Paczyński 1990) to compute the chemical composition profile in the radiative zones of the $M = 0.75$ and $1M_{\rm TO}$ parent stellar models. We evolved MS stars of total mass $M = 0.6$ and 0.8 $M_\odot$, primordial helium abundance $Y = 0.25$ and metallicity $Z = 0.001$ for a time $t \approx 15$ Gyr, which brought the center of the $M = 0.8$ $M_\odot$ star to the point of hydrogen exhaustion. Everywhere in the (fully convective) $M = 0.2$ and $0.5M_{\rm TO}$ stars, we set a constant fractional helium abundance $Y = 0.24$ and $Y = 0.25$, respectively. In the convective envelope of our $0.75M_{\rm TO}$ parent star, we set $Y = 0.25$. Figure 2 shows the resulting profiles, which are used to assign the helium abundance to all the SPH particles in the calculations. The final column in Table 1 gives the total mass fraction of helium $M_{\rm He}/M$ for each of the parent stars. Although the assumed composition profiles do not affect the hydrodynamics of a collision in any way, they are needed to determine the chemical composition profile of the merger remnant. In § 4.4 we present a method for applying our results to arbitrary initial composition profiles.

The stars are initially nonrotating and separated by at least 4 times the radius of the larger star, which allows tidal effects to be neglected in the initial configuration. The initial velocities are calculated by approximating the stars as point masses on an orbit with zero orbital energy and a pericenter separation r_p. The Cartesian coordinate system is chosen such that these hypothetical point masses of mass M_1 and M_2 would reach pericenter at positions $x_i = (-1)^i [1 - M_i/(M_1 + M_2)]r_p$, $y_i = z_i = 0$, where $i = 1, 2$ and $i = 1$ refers to the more massive star. The orbital plane is set to be $z = 0$. With these choices, the center of mass resides at the origin.

4. RESULTS

Table 2 summarizes the initial parameters and final results of all our calculations. The first column gives the name by which the calculation is referred to in this paper. The second and third columns give the masses M_1 and M_2 of the colliding stars, in units of $M_{\rm TO}$ (≈ 0.8 $M_\odot$). Column (4) gives the ratio $r_p/(R_1 + R_2)$, where r_p is the pericenter separation for the initial orbit and $R_1 + R_2$ is the sum of the two (unperturbed) stellar radii. This ratio has the value 0 for a head-on collision, and 1 for a grazing encounter. Note, however, that an encounter with $r_p/(R_1 + R_2) \gtrsim 1$ can still lead to a direct collision in the outer envelopes of the two stars because of the large tidal

TABLE 2

SUMMARY OF COLLISIONS

Case (1)	M_1 (2)	M_2 (3)	$\frac{r_p}{R_1 + R_2}$ (4)	r_0 (5)	t_f (6)	n_p (7)	$1 - \frac{M}{M_1 + M_2}$ (8)	$T/\lvert W\rvert$ (9)	V_x (10)	V_y (11)
A	1.00	1.00	0.00	4	22	1	0.064	0.00	0.000	0.000
B	1.00	1.00	0.25	4	48	3	0.023	0.07	0.000	0.000
C	1.00	1.00	0.50	5	85	4	0.012	0.12	0.000	0.000
D	1.00	0.75	0.00	5	15	1	0.057	0.00	−0.015	0.000
E	1.00	0.75	0.25	5	41	2	0.024	0.07	−0.003	−0.007
F	1.00	0.75	0.50	5	65	3	0.008	0.09	0.000	−0.002
G	1.00	0.50	0.00	5	30	1	0.056	0.00	−0.029	0.000
H	1.00	0.50	0.25	5	39	2	0.028	0.05	−0.010	−0.009
I	1.00	0.50	0.50	5	68	3	0.008	0.07	−0.001	−0.003
J	0.75	0.75	0.00	5	16	1	0.049	0.00	0.000	0.000
K	0.75	0.75	0.25	5	40	2	0.028	0.08	0.000	0.000
L	0.75	0.75	0.50	3	95	4	0.022	0.10	0.000	0.000
M.....	0.75	0.50	0.00	3	15	1	0.054	0.00	−0.034	0.000
N	0.75	0.50	0.25	3	40	2	0.029	0.05	−0.010	−0.011
O	0.75	0.50	0.50	3	62	3	0.010	0.07	−0.002	−0.002
P	0.50	0.50	0.00	1.85	14	1	0.037	0.00	0.000	0.000
Q	0.50	0.50	0.25	1.85	29	2	0.029	0.06	0.000	0.000
R	0.50	0.50	0.50	1.85	30	3	0.010	0.10	0.000	0.000
S.....	0.50	0.50	0.75	1.85	35	3	0.008	0.12	0.000	0.000
T	0.50	0.50	0.95	1.85	61	3	0.011	0.13	0.000	0.000
U	1.00	0.20	0.00	5	23	1	0.026	0.00	0.003	0.000
V	1.00	0.20	0.25	5	41	2	0.025	0.02	−0.009	−0.004
W.....	1.00	0.20	0.50	5	81	3	0.021	0.03	−0.007	−0.007

deformations near pericenter. We did not attempt to perform any calculations for $r_p/(R_1 + R_2) > 1$, for reasons discussed in § 5. Column (5) gives the initial separation r_0 in units of R_{TO}. Column (6) gives the final time t_f at which the calculation was terminated, in the units of equation (12); see § 2.3 for a discussion of how the values of t_f were obtained. Column (7) gives the number n_p of successive pericenter interactions that the stars experience before merging. In general, n_p increases with r_p, and it is only for very nearly head-on collisions that the two stars merge immediately after the first impact ($n_p = 1$ in that case). Column (8) gives the mass-loss fraction $1 - M/(M_1 + M_2)$, where M is the mass of the bound fluid in the final merged configuration. Column (9) gives the ratio $T/|W|$ of rotational kinetic energy to gravitational binding energy of the (bound) merger remnant in its center of mass frame at time t_f. Columns (10) and (11) give the velocity components V_x and V_y in the units of equation (13) for the merger remnant's center of mass at time t_f, in the system's center of mass frame ($V_z = 0$ by symmetry). Since the amount of mass ejected during a parabolic collision is very small, the merger remnant never acquires a large recoil velocity. The largest value of 0.035 in our calculations occurs for case M and corresponds to a physical speed of about 14 km s^{-1} (for $M_{TO} = 0.8\ M_\odot$ and $R_{TO} = R_\odot$). This may be large enough to eject the object from the cluster core but not to eject it from the entire cluster.

4.1. *Overview of the Results for Two Typical Cases*

One of our calculations involving two TAMS stars (Case C) has already been described by Lombardi et al. (1995). In this section we discuss in detail the results of two other representative cases (E and G).

Figure 3 illustrates the dynamical evolution for Case E: a TAMS star ($M_1 = M_{TO}$) collides with a slightly less massive star ($M_2 = 0.75M_{TO}$). The initial separation is $r_0 = 5$ and the parabolic trajectory has a pericenter separation $r_p = 0.25(R_1 + R_2)$. The first collision at time $t \approx 4$ disrupts the outer layers of the two stars but leaves their inner cores essentially undisturbed. The two components withdraw to apocenter at $t \approx 7$ and by $t \approx 10$ are colliding for the second, and final, time ($n_p = 2$). The merger remnant undergoes some large-amplitude oscillations that quickly damp away becasue of shock dissipation. Only about 2% of the total mass is ejected during the collision, and this ejection is nearly isotropic. As a result, the final recoil velocity of the merger remnant in the orbital plane is small, $V \approx 0.007$.

The final ($t = 41$) equilibrium configuration (see Fig. 4) is an axisymmetric, rapidly rotating object ($T/|W| = 0.07$). Figure 5 shows SPH-particle values of the angular velocity Ω as a function of the cylindrical radius ϖ (the distance to the rotation axis) in the equatorial plane. The uniformly rotating core contains only about 15% of the mass and is an artifact of the artificial viscosity, as discussed in § 4.2. The majority of fluid in the merger remnant is differentially rotating (e.g., $d\ln\Omega/d\ln\omega \approx -1.8$ at $\varpi = 3R_{TO}$). The angular velocity drops to half its central value near $\varpi = 1.1R_{TO}$, and 80% of the mass is enclosed within the isodensity surface with this equatorial radius.

Figure 6 displays the thermal energy U, kinetic energy T, gravitational potential energy W, and total energy $E = U + T + W$ as a function of time t for case E. The total energy is conserved to within 2%. Dips in the potential energy W correspond either to a collision of the two components before final merging or to a maximum contraction

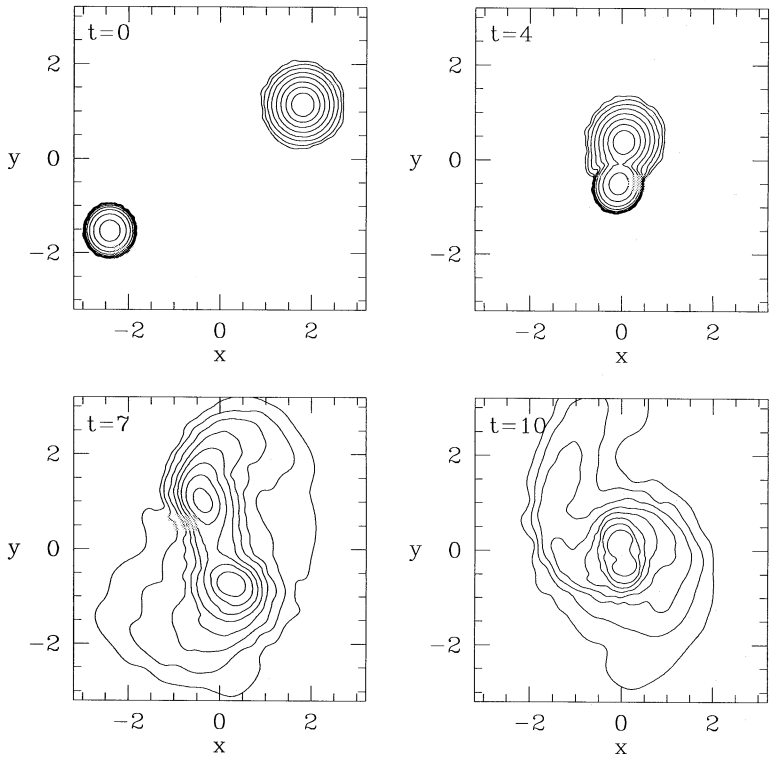

FIG. 3.—Snapshots of density contours in the orbital plane ($z = 0$) showing the dynamical evolution in case E, where we consider a parabolic collision between parent stars of masses $M_1 = M_{TO}$ and $M_2 = 0.75M_{TO}$ at a pericenter separation $r_p = 0.25(R_1 + R_2)$. There are eight density contours, which are spaced logarithmically and cover four decades down from the maximum.

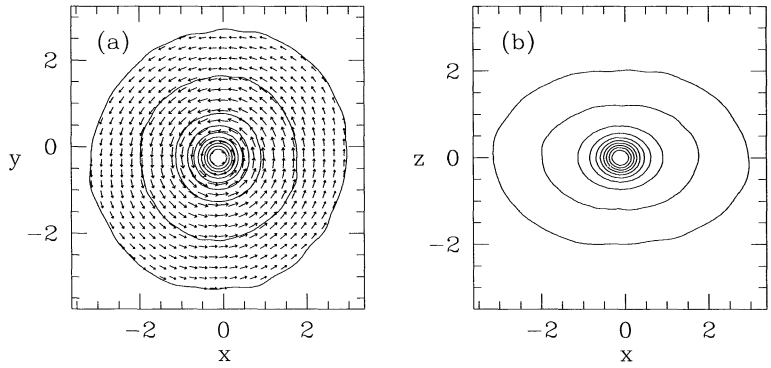

FIG. 4.—Density contours and velocity field for the final ($t = 41$) configuration of the case E collision in (*a*) the equatorial ($z = 0$) plane and (*b*) the $y =$ constant plane, which includes the rotation axis. There are 10 contours such that, starting from the center, each corresponding isodensity surface encompasses an additional 10% of the total mass, with the exception of the outermost contour, which encompasses 95% of the mass.

during the subsequent oscillations of the merger remnant. The criterion we use to distinguish collisions (which should be included in the number of interactions n_p before the stars merge) from oscillations is that the first local maximum of W which is lower than the previous local maximum occurs immediately after the final merging. The idea behind this criterion is that a collision without merger ultimately tends to increase the system's gravitational potential energy, whereas a merger will decrease the potential energy. For example, in Figure 6, the local maximum of W at $t \approx 11$ is lower than the one at $t \approx 6$, so that the dips in W at $t \approx 4$ and 11 account for the number $n_p = 2$ of interactions given in Table 2 for case E. The remaining dips at $t \approx 12$ and 15 correspond to the peak contraction of the merger remnant during oscillations. The value $n_p = 2$ obtained here in this way agrees with what one gets simply by direct visual inspection of the system at various times. In some cases, however, visual inspection can be subjective, since it is often difficult to recognize two components connected by a bridge of high-density material just prior to final merging.

Figure 7 illustrates the dynamical evolution in case G, which involves a TAMS star ($M_1 = M_{TO}$) and a low-mass MS star with $M_2 = 0.5M_{TO}$ on a head-on parabolic trajectory with initial separation $r_0 = 5$. The initial collision occurs at time $t \approx 4$, and the stars never separate. The resulting isodensity surfaces of the final equilibrium configuration are essentially spherically symmetric (Fig. 8). About 6% of the total mass becomes gravitationally unbound following the collision, and it is ejected preferentially in the $+x$-direction. Of this ejected material, 95% originated in the more massive ($M = M_{TO}$) star.

Figures 9*a* and 9*b* show the entropy profiles for the final configurations in cases E and G. Except over the outer few percent of the mass, where equilibrium has not yet been reached (see § 2.3), the specific entropy s is an increasing function of the interior mass fraction m/M. Here m is the mass inside an isodensity surface, and M is the total bound mass of the merger remnant. Most of the scatter of the points in Figure 9 is physically meaningful, since isodensity surfaces and surfaces of constant entropy do not coincide.

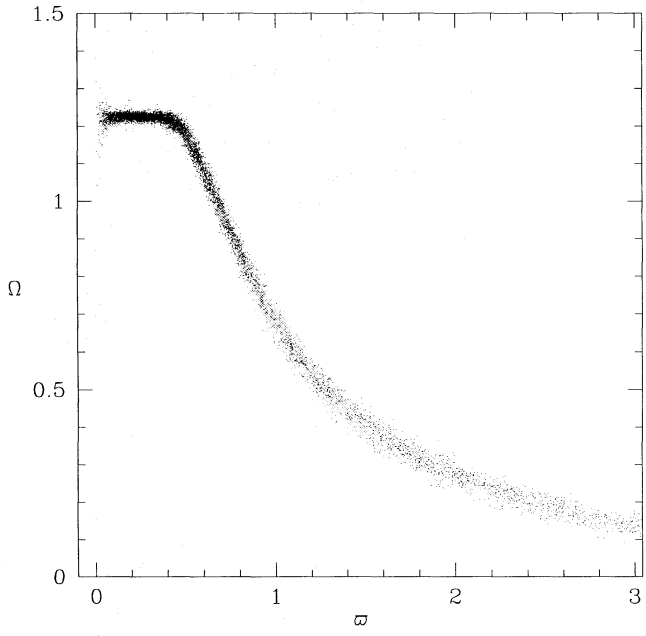

FIG. 5.—Angular velocity Ω as a function of cylindrical radius ϖ for particles near the equatorial plane ($|z_i| < 2h_i$, where h_i is the particle smoothing length) in the final ($t = 41$) merger remnant of case E.

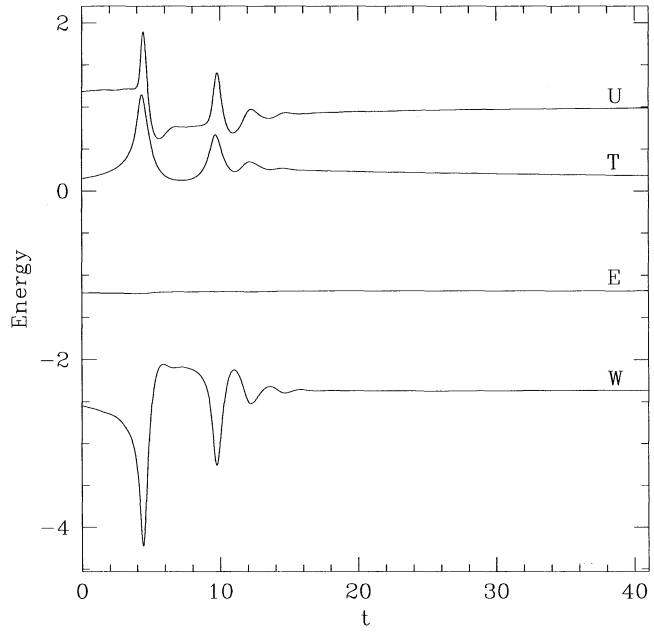

FIG. 6.—Internal energy U, kinetic energy T, gravitational potential energy W, and total energy $E = U + T + W$ as a function of time t for case E.

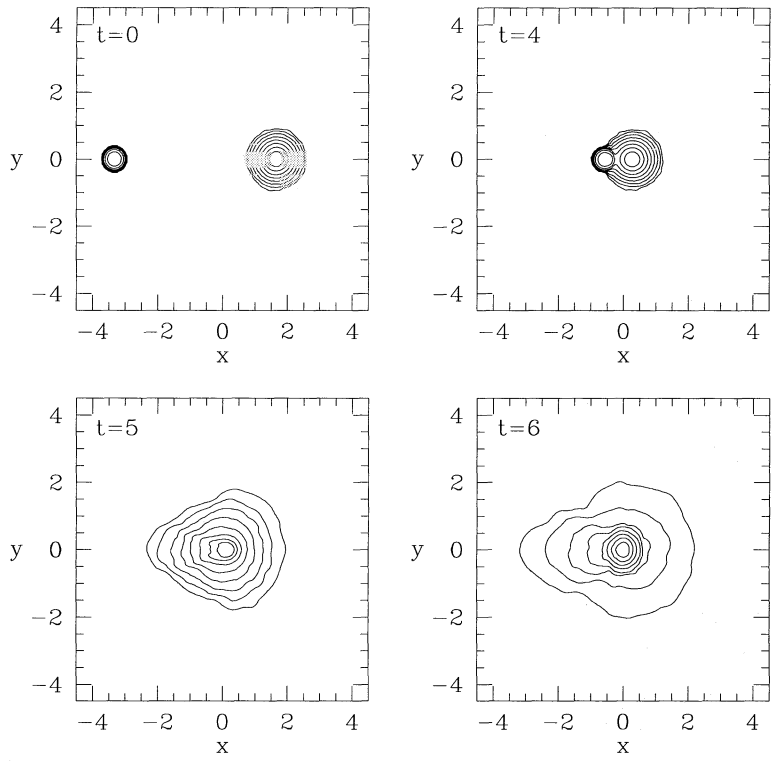

FIG. 7.—Snapshots of density contours in the orbital plane ($z = 0$) showing the dynamical evolution in case G, where we consider a head-on parabolic collision between parent stars of masses $M_1 = M_{TO}$ and $M_2 = 0.5M_{TO}$. There are eight density contours, which are spaced logarithmically and cover four decades down from the maximum.

The small scatter in Figure 9*b* demonstrates that the entropy does tend toward spherical symmetry in nonrotating merger remnants, despite the strong angular dependence of the shock heating owing to the geometry of the collision.

Even though the density and entropy profiles of both the merger remnant and parent stars are spherically symmetric in case G, this does not imply that the chemical composition must also share this symmetry. Indeed, the effects of anisotropic shock heating are always evident in the final spatial distribution of the chemical composition. On a constant-entropy surface in the final configuration, particles that have been shock heated the most necessarily had the lowest entropy prior to the collision. Since lower entropy material generally has higher helium abundance (see Figs. 1 and 2), shock-heated regions tend to have higher helium abundances. Generally, fluid elements that reside in the orbital plane, and especially those which lie along the collision axis in $r_p = 0$ cases, are shielded the least from the shock. Figure 10 displays the angular distribution of the helium abundance for the merger remnants of cases E and G, near the interior mass fractions $m/M = 0.25$, 0.5, and 0.75. The helium abundance Y peaks in Figures 10*b* and 10*d* at the polar angle $\theta = \pi/2$ (the equatorial plane), as well as in Figure 10*c* at $\phi = 0$ (the collision axis). In the $r_p \neq 0$ cases, shear in the differentially rotating merger remnant tends to make the profiles axisymmetric (see Fig. 10*a*). However, no dynamical motions exist to circulate the fluid along the meridional directions, and consequently, on an isodensity surface the fractional helium abundance increases from the poles to the equators for both rotating and nonrotating merger remnants (see Figs. 10*b* and 10*d*). Meridional circulation will smooth out these deviations from compositional spherical symmetry over a timescale

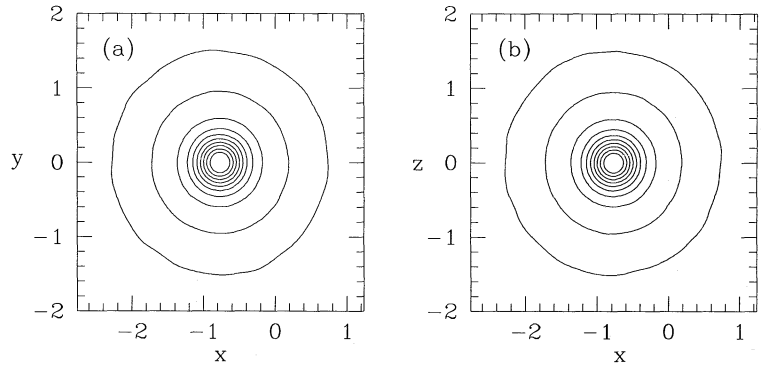

FIG. 8.—Cross sections of isodensity surfaces for the final ($t = 30$) configuration of the case G collision in (*a*) the equatorial ($z = 0$) plane and (*b*) the y = constant plane, which includes the rotation axis. The 10 contours are spaced the same as in Fig. 4.

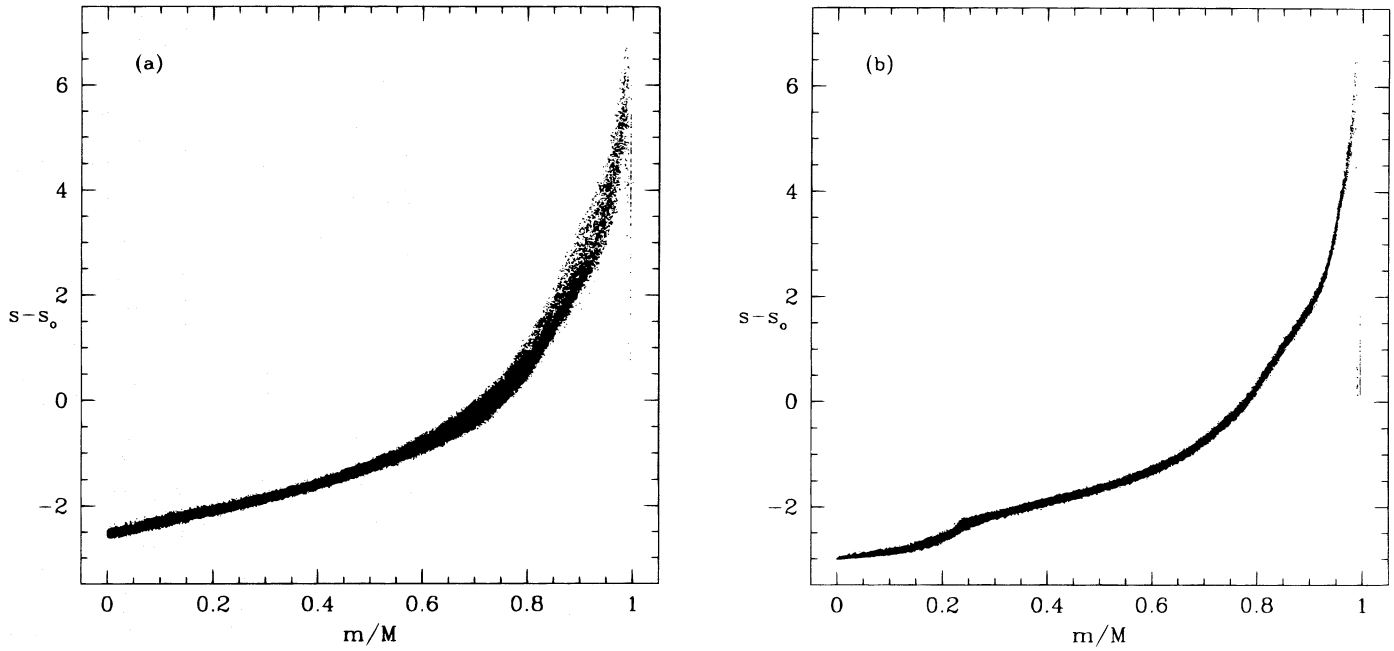

FIG. 9.—Relative specific entropy $s - s_0$ as a function of final mass fraction m/M for the merger remnants of (*a*) case E and (*b*) case G. Here m is the mass enclosed by an isodensity surface and M is the total bound mass of the merger remnant.

much longer than that treatable by our purely dynamical code (see related discussion in § 5). As a practical concern, we note that stellar evolution codes, which can use our merger remnants as initial data, usually assume spherical symmetry. For these reasons, we often average out the angular dependence when presenting composition, and other, profiles.

Figures 11*a* and 11*b* show the helium mass fraction Y as a function of the interior mass fraction m/M for the final merged configurations of cases E and G, respectively. The points correspond to the final SPH particle values, with the long-dashed curve representing their average. The spread in the points is caused by the mixing of the fluid as well as the deviation from spherical symmetry. Only a small fraction of the observed mixing is a numerical artifact of the SPH scheme (see § 4.5). In case E (Fig. 11*a*), there is only a modest amount of hydrogen in the core, with the innermost 25% of the mass being 60% helium. For both cases E and G, it is immediately apparent that the helium enrichment in the outer layers is minimal since the fractional helium abundance is just barely above $Y = 0.25$, the value in the outer layers of the parent stars.

The horizontal line at the bottom of Figure 11*b* corresponds to the particles in case G, which originated in the less massive parent star, star 2, all of which have a helium abundance $Y = 0.25$. Although these particles are spread over the entire range $0 < m/M < 1$ in the merger remnant, they are found preferentially near the center. Of all the particles that originated in star 2, 69% ultimately end with $m/M < 0.25$, while only 6% end in the range $0.75 < m/M < 1$. Essentially, the entire star 2 has sunk to the center of the merger remnant, displacing the material in star 1 and leaving only a small amount of shock-heated gas in the remnant's outer envelope. Consequently, the hydrogen enrichment in the core is quite pronounced: all of the innermost 22% of the mass originated in star 2 and is therefore 75% hydrogen. This core concentration of hydrogen is even higher than would be obtained if the stars had been completely mixed by the collision (64% hydrogen). Also note that the average helium abundance jumps to a maximum exceeding $Y = 0.7$ near $m/M = 0.3$. The subsequent stellar evolution of an object with such an atypical chemical abundance profile could be quite peculiar (see § 5).

4.2. *Rotational Properties of the Merger Remnants*

The collisions with $r_p \neq 0$ result in rapidly, differentially rotating merger remnants. As a global measure of rotation, we list in Table 2 the final values of $T/|W|$, the ratio of kinetic energy to gravitational binding energy, for the merger remnants. Rotating fluid configurations with $T/|W| \gtrsim 0.14$ are secularly unstable, and those with $T/|W| \gtrsim 0.26$ are dynamically unstable (Chandrasekhar 1969; Shapiro & Teukolsky 1983, chap. 7). Our final merged configurations are, by definition, dynamically stable, but they could in principle be secularly unstable. Although some of our calculations produce merger remnants close to the secular stability limit, none of them exceed it. However, extrapolation of our results to larger values of r_p suggests that secular instabilities could well develop in some merger remnants.

Table 3 lists the values of the central angular velocity Ω_0 in the equatorial plane as well as other quantities characterizing the rotation in the outer layers of the merger remnants. Specifically, for the two mass fractions $m/M = 0.9$ and $m/M = 0.95$, we give the values of the polar and equatorial radii r_p and r_e, the angular velocity Ω in the equatorial plane, and the ratio $\Omega^2 r_e/g$ of centrifugal to gravitational acceleration in the equatorial plane. We see that $\Omega^2 r_e/g$ can be a significant fraction of unity, indicating that some configurations are rotating near breakup. The central angular velocity Ω_0 is typically an order of magnitude larger than the angular velocity Ω at $m/M = 0.95$.

Figure 12 shows contours of the specific angular momentum $\Omega\varpi^2$, where ϖ is the cylindrical radius measured from the rotation axis, in the vertical (x, z) plane for several representative cases. The outermost bounding curves corre-

1996ApJ...468..797L

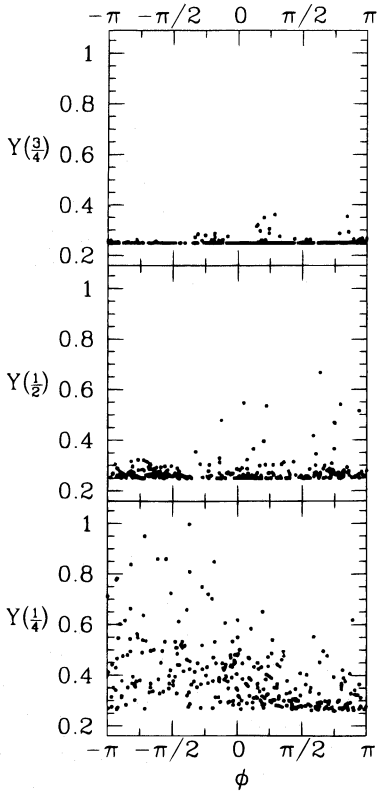

FIG. 10a

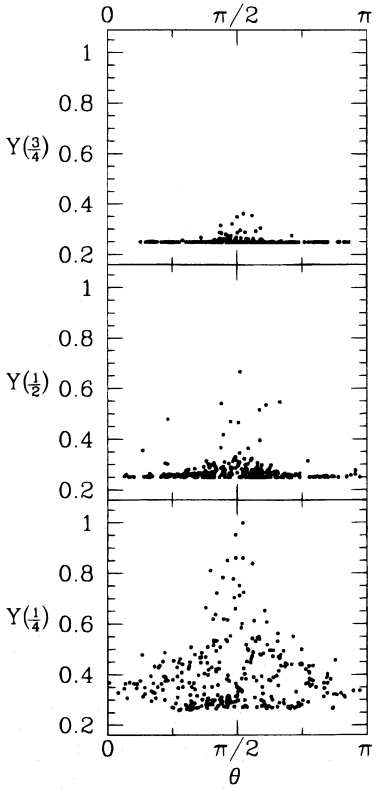

FIG. 10b

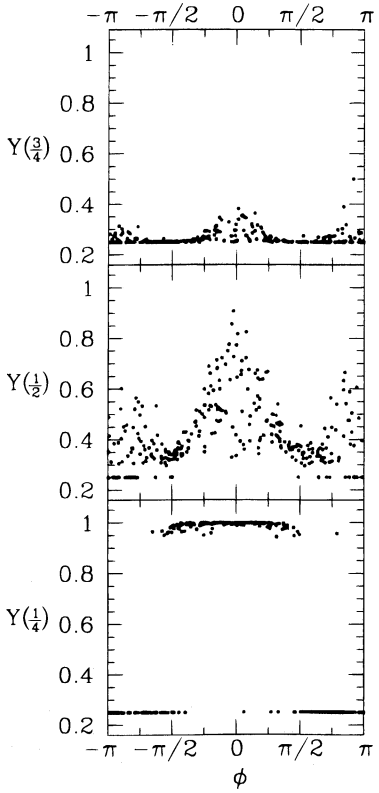

FIG. 10c

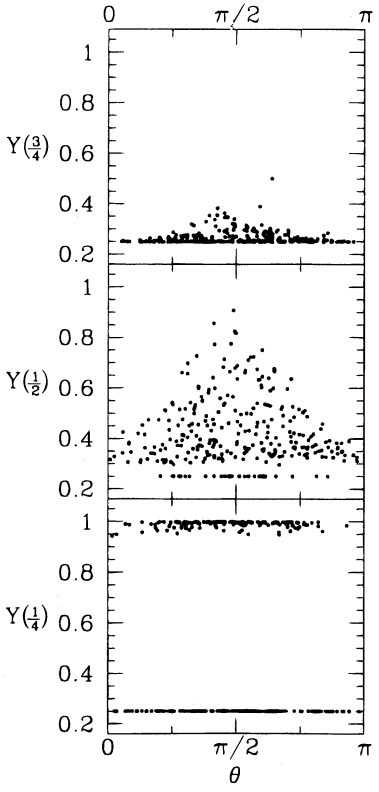

FIG. 10d

FIG. 10.—Fractional helium abundance Y for particles in the vicinity of the final mass fractions $m/M = \frac{1}{4}, \frac{1}{2}$, and $\frac{3}{4}$ as a function of the azimuthal angle ϕ (measured counterclockwise from the positive x-direction) and the polar angle θ (measured from the rotation axis). Panels (*a*) and (*b*) are for the merger remnant of case E, while panels (*c*) and (*d*) are for case G.

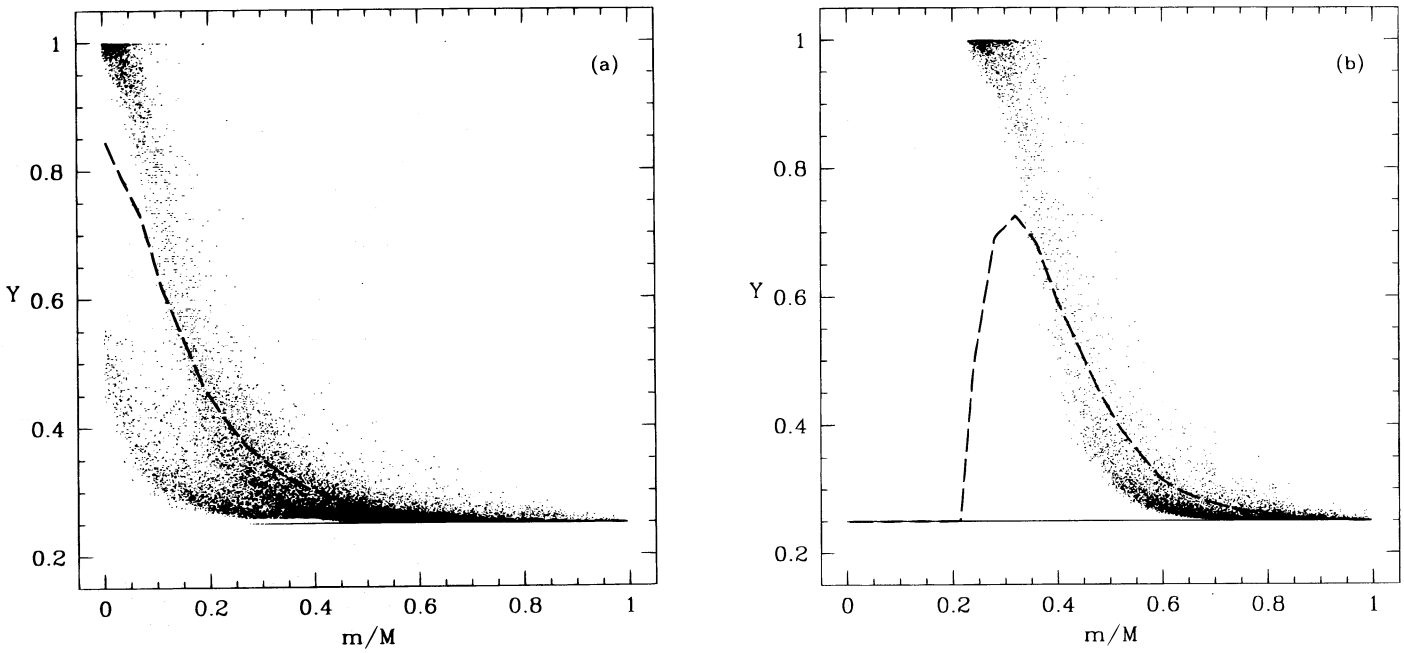

FIG. 11.—Fractional helium abundance Y as a function of final mass fraction m/M for the merger remnants of (*a*) case E and (*b*) case G. The dashed line represents the average of the individual SPH particle values.

spond to $m/M = 0.95$. Clearly, the merger remnants are not barotropic since the condition $d\Omega/dz = 0$ is not satisfied everywhere. The implications of this result will be discussed in § 5.

Artificial viscosities of the form of equation (9) with $\alpha \gtrsim 1$ introduce a large shear viscosity into the fluid. The consequences of shear viscosity will be discussed in detail in a future paper (Lombardi et al. 1996), but here we summarize the main effects relevant to our present calculations. One prominent effect is for a uniformly rotating core to develop in our merger remnants, as seen in Figure 5. With time, the core grows in size, and the central angular velocity Ω_o drops. For instance in case E, the uniformly rotating core has $\Omega = \Omega_o = 1.6$ for all $\varpi \lesssim 0.2$ at $t = 25$, while $\Omega = \Omega_o = 1.2$ for $\varpi \lesssim 0.4$ at $t = 41$ (see Fig. 5). The angular velocity of the outer layers increases slightly as a result, since the total angular momentum of the system is conserved. Furthermore, the ratio of kinetic to gravitational binding energy $T/|W|$ drops slightly. Since the decrease in Ω_o and $T/|W|$ would not occur in a simulation free of shear viscosity, the values of Ω_o in Table 3 and $T/|W|$ in Table 2 should be interpreted as lower limits. Note, however, that it may not be physically unrealistic to have such a large shear viscosity. Indeed, it is well known that in most real rotating systems (such as accretion disks), rapid and differential rotation can induce a large anomalous shear viscosity.

TABLE 3

ROTATION OF MERGER REMNANTS

		$m/M = 0.9$				$m/M = 0.95$			
CASE	Ω_0	r_p	r_e	Ω	$\Omega^2 r_e/g$	r_p	r_e	Ω	$\Omega^2 r_e/g$
A	0.0	1.2	1.2	0.00	0.00	2.0	2.0	0.00	0.00
B	1.2	1.6	2.5	0.21	0.36	2.6	4.0	0.10	0.33
C	1.5	1.2	2.5	0.27	0.57	2.1	3.8	0.13	0.45
D	0.0	1.2	1.2	0.00	0.00	2.0	2.0	0.00	0.00
E	1.2	1.2	1.9	0.31	0.40	2.0	3.0	0.14	0.32
F	1.2	1.2	2.5	0.27	0.67	1.8	3.9	0.13	0.59
G	0.0	0.9	1.0	0.00	0.00	1.5	1.5	0.00	0.00
H	1.2	1.0	1.5	0.40	0.40	1.7	2.5	0.17	0.29
I	1.2	1.0	2.0	0.34	0.61	1.6	3.3	0.16	0.58
J	0.0	1.3	1.3	0.00	0.00	2.0	2.0	0.00	0.00
K	1.2	1.1	1.7	0.32	0.34	1.9	2.7	0.14	0.26
L	1.3	1.2	2.3	0.23	0.44	2.4	3.7	0.11	0.37
M.....	0.0	1.0	1.0	0.00	0.00	1.6	1.6	0.00	0.00
N	1.2	0.9	1.3	0.39	0.30	1.6	2.2	0.15	0.21
O	1.3	1.0	1.8	0.30	0.43	1.7	2.9	0.13	0.34
P	0.0	0.9	0.9	0.00	0.00	1.4	1.4	0.00	0.00
Q	1.5	0.7	1.0	0.53	0.29	1.2	1.7	0.21	0.20
R	1.8	0.7	1.2	0.50	0.46	1.1	1.8	0.24	0.37
S.....	1.8	0.6	1.5	0.45	0.66	0.9	2.0	0.26	0.57
T	2.1	0.5	1.4	0.45	0.65	0.8	2.3	0.22	0.63
U	0.0	0.8	0.8	0.00	0.00	1.1	1.1	0.00	0.00
V	0.7	0.9	1.0	0.44	0.20	1.4	1.8	0.20	0.20
W.....	0.8	0.9	1.2	0.47	0.32	1.5	2.4	0.17	0.33

With the artificial viscosity parameters $\alpha \gtrsim 1$ and $\beta \sim 1$, the term linear in μ_{ij} in equation (9) dominates in the absence of shocks, and the angular momentum transfer timescale in a differentially rotating configuration can be comparable to the dynamical timescale. For a region in which the angular velocity profile obeys $\Omega \propto \varpi^{-\lambda}$, dimensionless analysis on the Π_{ij} term in equation (8) gives a viscous timescale $\sim \varpi (N_N)^{1/2}/(\alpha\lambda c_s)$. In the units defined in § 2.2, the sound speed $c_s \sim 1$ throughout our merger remnants. Furthermore, we have $\alpha = 1$ in our simulations, and our results imply $\lambda \sim 1$. Therefore, at $\varpi \approx 1$, the viscous timescale is only an order of magnitude larger than the dynamical timescale, meaning that the rotation profile in the region $\varpi \lesssim 1$ is significantly affected by shear viscosity within only ~ 10 time units. Note that for $\alpha = 0$, the viscous timescale becomes $\sim \varpi (N_N)^{1/2}/(\beta\lambda^2\Omega h)$, where h is a typical smoothing length of a local SPH particle. We have completed a simulation analogous to case E, but with $\alpha = 0$ and $\beta = 2.5$ instead of $\alpha = 1$ and $\beta = 2$. The viscous timescale in the $\alpha = 0$ simulation is more than an order of magnitude larger in the remnant's core than in case E. This difference in timescales is evident in the resulting rotation profile: at $t = 41$, the central angular velocity $\Omega_o = 1.7$, as opposed to the $\Omega_o = 1.2$ found in case E (see Fig. 5). All other profiles,

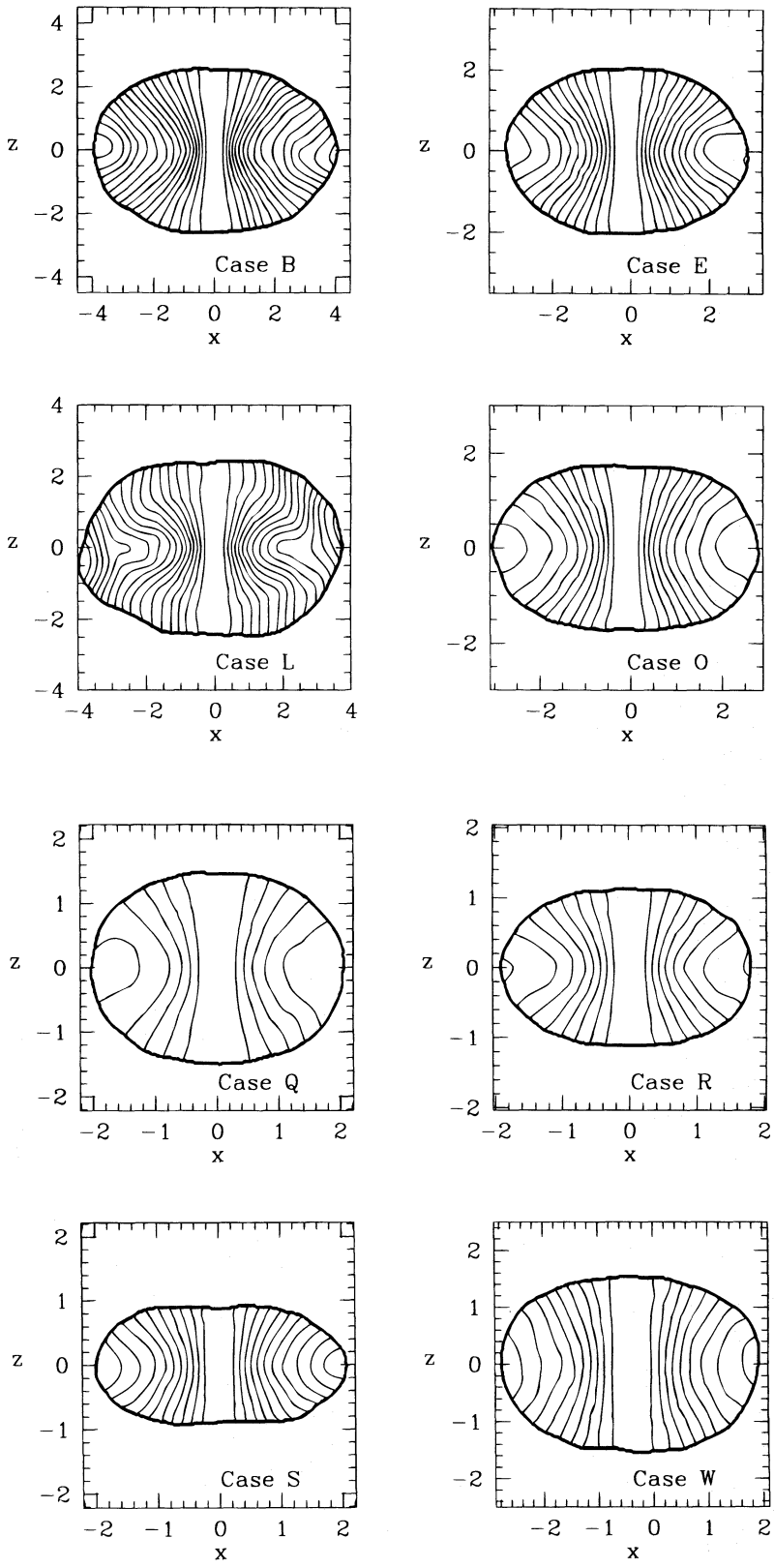

FIG. 12.—Contours of the specific angular momentum $\Omega\varpi^2$ in the vertical (x, z) plane (meridional section) for several representative cases. Here Ω is the angular velocity and ϖ is the cylindrical radius measured from the rotation axis. The contours have a linear spacing of 0.1, with the specific angular momentum increasing from the rotation axis to the outer layer of the merger remnant. The thick bounding curve marks the isodensity surface, which encloses 95% of the total gravitationally bound mass.

such as entropy and chemical composition, are only weakly dependent on the values of the artificial viscosity parameters α and β. Entropy production due to the shear viscosity does of course occur in the merger remnant, but only on a timescale much larger than the timescale for angular momentum transfer (as can be seen from dimensional analysis on eq. [11]). Chemical composition profiles, when expressed as a function of interior mass fraction, are hardly affected by the shear viscosity.

4.3. *Composition and Thermodynamic Profiles*

Figures 13*a*–13*g* show the variation of the density ρ, relative specific entropy $s - s_o$, helium fraction Y, and temperature T as a function of m/M for all merger remnants. The density and entropy profiles are fundamental in the sense that they do not depend on the assumed initial helium profiles. The entropy and helium profiles have been averaged over isodensity surfaces. The temperature profile is calculated from the entropy and helium profiles by setting the pressure $p = \rho kT/\mu$ equal to $p = A\rho^{\Gamma_1}$, solving for T and using equation (4). Here the mean molecular weight μ is given by

$$\mu = m_{\rm H}(2X + \tfrac{3}{4}Y + \tfrac{1}{2}Z)^{-1} , \tag{17}$$

where $m_{\rm H}$ is the mass of hydrogen and X, Y, and Z are the fractional abundances of hydrogen, helium and metals. For Population II stars, $Z \sim 10^{-4}$–10^{-3}, and the precise value does not significantly affect the calculated temperature profiles.

Note the peculiar shapes of some of the temperature and helium profiles in Figure 13. For example, often the temperature or helium abundance reaches its maximum value somewhere other than the center of the star. Although these configurations are very close to hydrostatic equilibrium, it is clear that they are not in thermal equilibrium (see related discussion in § 5). These unusual profiles suggest that we look at the condition for convective stability more carefully. For a nonrotating star, this condition can be written simply as

$$\frac{ds}{dr} > 0 , \tag{18}$$

where s is the local specific entropy (see, e.g., Landau & Lifshitz 1959, § 4). When written in terms of temperature and composition gradients, equation (18) becomes, for an ideal gas,

$$\frac{1}{T}\frac{dT}{dr} > \frac{1}{T}\left(\frac{dT}{dr}\right)_{ad} + \frac{1}{\mu}\frac{d\mu}{dr} , \tag{19}$$

which is known as the Ledoux criterion (see, e.g., Kippenhahn & Weigert 1990, chap. 6). Here the subscript *ad* denotes that the derivative is to be taken at constant entropy. Most of our merger remnants have composition gradients, and it is in the regions where $d\mu/dr > 0$ that equation (19) can require $dT/dr > 0$ for stability. For chemically homogeneous stars, the second term on the right-hand side of equation (19) vanishes, and the familiar Schwarzschild criterion results. Although equation (18) is quite general, it does require slight modification for rotating stars (see Tassoul 1978, chap. 7).

Figure 13*a*, 13*d*, and 13*f* demonstrate that merger remnants formed from equal-mass parent stars have composition profiles that mimic those of the parents, as can be seen by comparing the resulting helium profiles to the corresponding parent profiles in Figure 2. In Figure 13*f*, all of the merger remnants have $Y = 0.25$ for all m/M, which is simply because the fully convective parents stars in these cases had $Y = 0.25$ everywhere.

We see from Figure 13*c* that the central specific entropy of the merger remnants increases with r_p, which can explain the qualitatively different shapes of the corresponding helium abundance profiles. This increase occurs because the number of interactions n_p, and hence the level of shock heating in star 2 (the smaller star), increases with r_p. The shock heating in the central region of star 1 is less sensitive to n_p, since the outer envelope absorbs the brunt of the shock. For case G (*solid line*), $n_p = 1$ and much of star 2 is able to maintain a lower specific entropy than the minimum value in star 1. Since low-entropy material tends to sink to the bottom of the gravitational potential well, the merger remnant's core consists entirely of fluid originally from star 2 and therefore with a helium abundance $Y = 0.25$. For case H (*long-dashed line*), $n_p = 2$ and, although the central fractional helium abundance is still 0.25, there is enough shock heating for the fluid at small m/M to be affected by contributions from both stars. For case I (*short-dashed line*), $n_p = 3$ and the additional shock heating is sufficient to prevent most of the fluid from star 2 from reaching the center of the remnant, which consequently is not significantly replenished with hydrogen.

Figure 13*g* displays the profiles for merger remnants resulting from collisions between two stars of masses $M_1 = M_{\rm TO}$ and $M_2 = 0.2M_{\rm TO}$. In the head-on case, the less massive star (star 2) plummets so quickly to the center that there is significant shock heating in the core of star 1, where the highest fractional helium abundance resides. This causes the helium-rich material to be spread throughout a larger region of the merger remnant, and the resulting helium profile is not as sharply peaked as in cases V and W.

4.4. *A Simplified Method for Calculating Final Profiles*

To make our results more useful to future studies, we now present a simple and general method for constructing the final composition profiles in our merger remnants for any assumed initial composition profiles. From our results, we extract some simple functions that can be applied to transform, for example, any given helium abundance profiles for the parents into a helium abundance profile for the merger remnant. Indeed, these transfer functions allow one to find the final profile of any passively advected quantity, provided only that the profiles of that quantity in the parent stars are both known and spherically symmetric.

Table 4 and Figure 14 establish a correlation between the initial and final mass fractions of an SPH particle and also demonstrate that the details of fluid mixing during a collision can be quite complicated. Table 4 presents mixing data for all eleven collisions between equal-mass stars. The parent stars and merger remnant are partitioned into zones according to interior mass fractions. For every zone in the final configuration, we list the fraction of particles that originated in each of the initial zones. Although there is definitely a preferred final mass fraction m/M for a given initial mass fraction m_i/M_i, there is always a range of m/M obtainable. In Figure 14, which is for case G, this range of mass fractions is evident in the spread of points around a preferred average. The lower band of points surrounding the solid line correspond to particles that originated in star 1, while the upper band surrounding the dashed line corre-

1996ApJ...468..797L

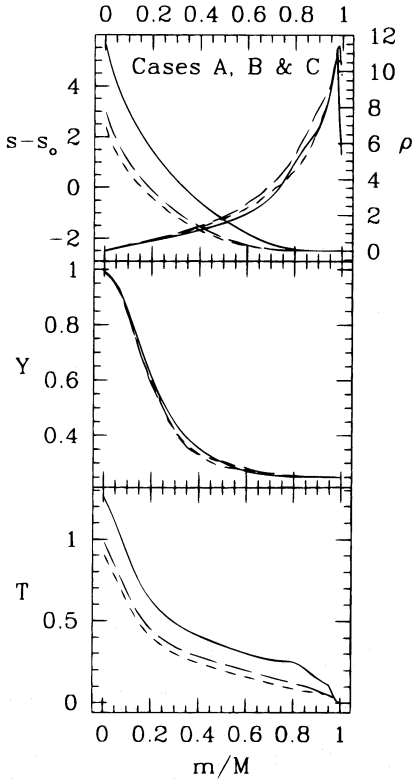

FIG. 13*a*

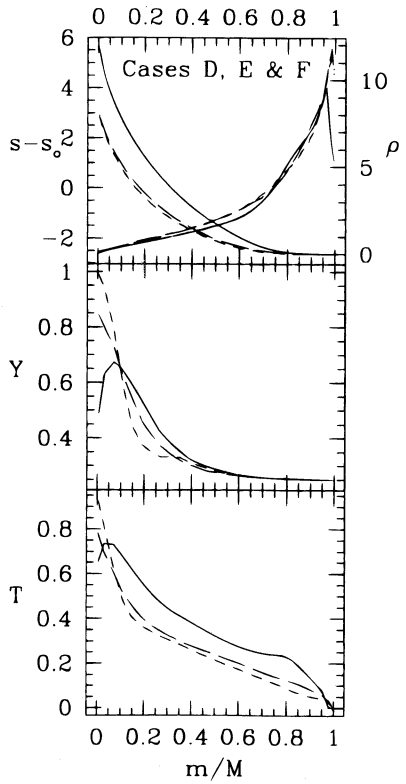

FIG. 13*b*

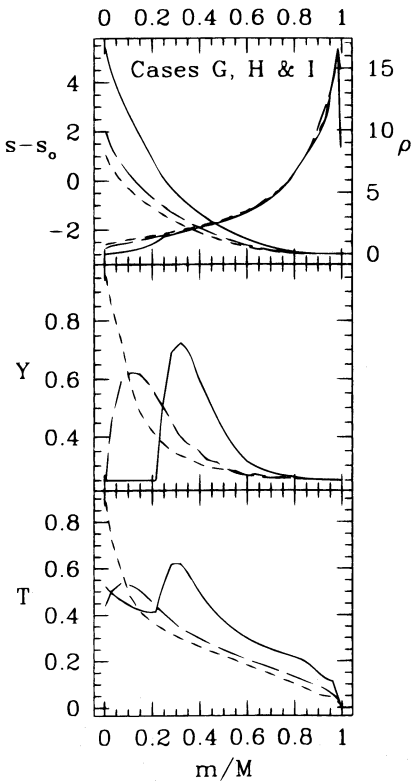

FIG. 13*c*

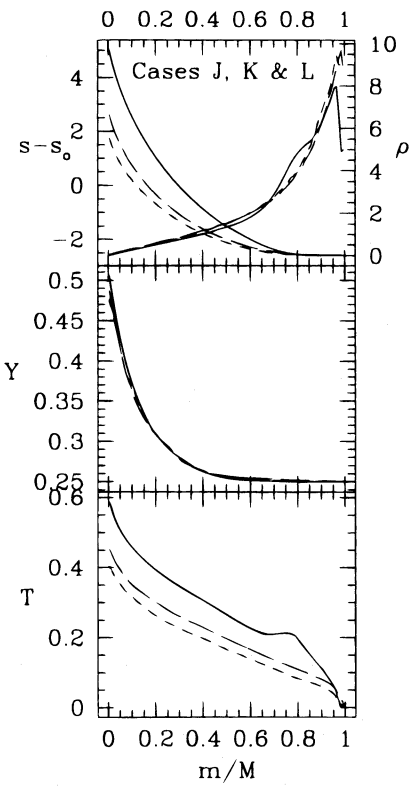

FIG. 13*d*

FIG. 13.—Interior profiles of the final merger remnants. The density ρ, relative specific entropy $s - s_o$, fractional helium abundance Y, and temperature T are shown for the following cases: (*a*) A, B, and C; (*b*) D, E, and F; (*c*) G, H, and I; (*d*) J, K, and L; (*e*) M, N, and O; (*f*) P, Q, R, S, and T; and (*g*) U, V, and W. The solid, long-dashed, and short-dashed lines correspond to collisions with pericenter separation $r_p = 0$, 0.25 and $0.5(R_1 + R_2)$, respectively. In (*f*), the dot-dashed and dotted lines represent cases S and T, which have $r_p = 0.75$ and $0.95(R_1 + R_2)$, respectively. The density and specific entropy profiles are plotted in the same frame (ρ is maximum at $m/M = 0$, while s is minimum there). The units are discussed in § 2.2.

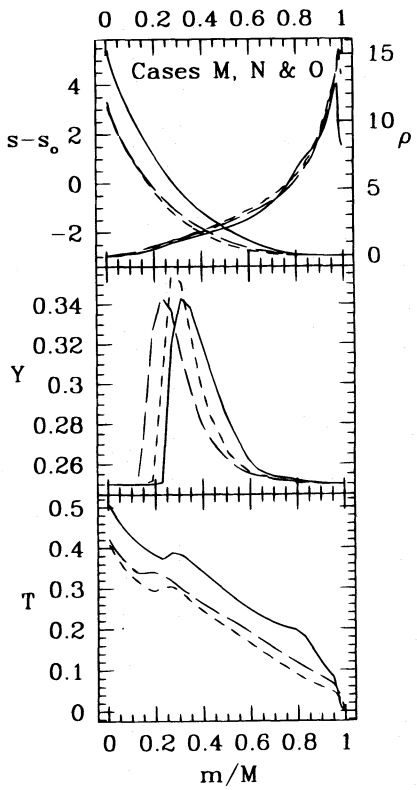

FIG. 13*e*

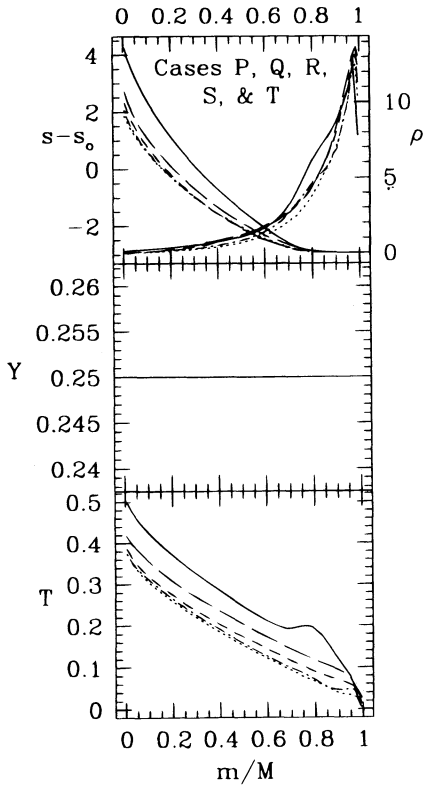

FIG. 13*f*

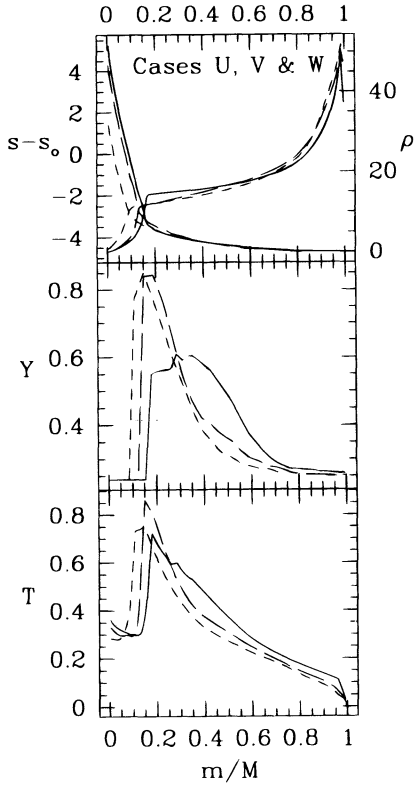

FIG. 13*g*

spond to particles that originated in star 2. The lines correspond to the average initial mass fraction $\langle m_i/M_i \rangle$ for stars $i = 1, 2$ as a function of the final mass fraction m/M, obtained by binning in the m/M dimension. In contrast, note that if the parent stars were completely mixed by the collision then the points would be distributed uniformly over the entire plot with an average initial mass fraction $\langle m_i/M_i \rangle = \frac{1}{2}$ for all m/M.

Let us define $p_1 = p_1(m/M)$ to be the probability that a particle with final mass fraction m/M originated in star 1. Obviously, $1 - p_1$ is then the probability that the particle originated in star 2. With this definition we can approximate the final profile of any passively advected quantity Q according to

$$Q\left(\frac{m}{M}\right) \approx p_1\left(\frac{m}{M}\right) Q_1\left(\left|\left\langle \frac{m_1}{M_1} \right\rangle\right|_{m/M}\right) + \left[1 - p_1\left(\frac{m}{M}\right)\right] Q_2\left(\left|\left\langle \frac{m_2}{M_2} \right\rangle\right|_{m/M}\right), \quad (20)$$

where Q_i are the initial (spherically symmetric) profiles for that quantity in the parent stars $i = 1, 2$. The quantities $\langle m_i/M_i \rangle|_{m/M}$ which appear in equation (20) are the average initial mass fractions, such as the ones in Figure 14, evaluated at the final mass fraction m/M. If all particles at m/M came from a single value of m_i/M_i, then equation (20) would be exact. In addition, if the initial profiles are linear over the range of m_i/M_i which contributes to the abundance at m/M, then the above relationship is exact.

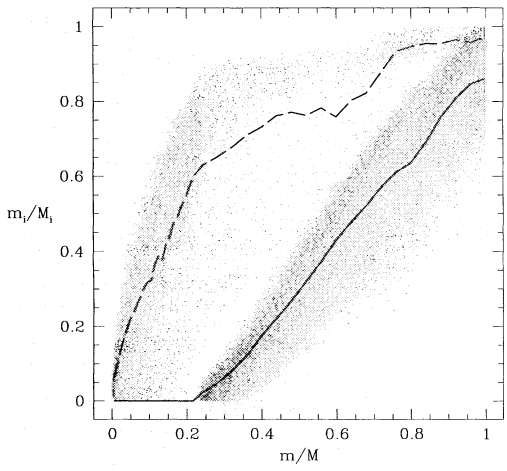

FIG. 14.—Individual points show the initial mass fraction m_i/M_i of SPH particles that originated in star $i = 1$ (the more massive star) or $i = 2$ (the less massive star) as a function of the particles' final mass fraction m/M for case G. The lines represent averages $\langle m_i/M_i \rangle$ obtained by binning in m/M, with the solid line corresponding to star 1 and the dashed line corresponding to star 2.

Figures 15*a*–15*g* give the average mass fractions $\langle m_i/M_i \rangle$ as a function of m/M for all of our collisions, while Figure 16 gives the function $p_1 = p_1(m/M)$ for the 12 collisions that involve parent stars of unequal mass. Collisions involving two identical stars necessarily have $\langle m_1/M_1 \rangle = \langle m_2/M_2 \rangle$ and $p_1 = \frac{1}{2}$ for all m/M. The solid, long-dashed, and short-dashed lines correspond to pericenter separations r_p of 0, 0.25, and $0.5(R_1 + R_2)$, respectively; in Figure 15*f* the dot-dashed and dotted lines refer to case S [$r_p = 0.75(R_1 + R_2)$] and case T [$r_p = 0.95(R_1 + R_2)$], respectively. Note that the horizontal line $\langle m_i/M_i \rangle = \frac{1}{2}$ would correspond to the fluid of star i being completely mixed throughout the merger remnant, which is not the case for any of our calculations. For collisions involving equal-mass stars, if there were no shock heating and no mass loss, then every particle would

TABLE 4

FLUID MIXING IN EQUAL PARENT MASS CASES

CASE	INITIAL MASS FRACTION	FINAL MASS FRACTION					
		0–0.01	0–0.25	0.25–0.5	0.5–0.75	0.75–1	Ejecta
A.....	0–0.25	1.00	0.91	0.16	0.00	0.00	0.00
	0.25–0.5	0.00	0.09	0.74	0.23	0.01	0.00
	0.5–0.75	0.00	0.00	0.10	0.69	0.28	0.01
	0.75–1	0.00	0.00	0.00	0.08	0.72	0.99
B.....	0–0.25	1.00	0.87	0.13	0.02	0.00	0.00
	0.25–0.5	0.00	0.13	0.65	0.23	0.02	0.00
	0.5–0.75	0.00	0.00	0.22	0.57	0.22	0.00
	0.75–1	0.00	0.00	0.00	0.18	0.75	1.00
C.....	0–0.25	1.00	0.88	0.13	0.01	0.00	0.00
	0.25–0.5	0.00	0.12	0.63	0.25	0.01	0.00
	0.5–0.75	0.00	0.00	0.24	0.51	0.26	0.00
	0.75–1	0.00	0.00	0.00	0.24	0.73	1.00
J.....	0–0.25	1.00	0.91	0.14	0.00	0.00	0.00
	0.25–0.5	0.00	0.09	0.75	0.20	0.01	0.00
	0.5–0.75	0.00	0.00	0.11	0.67	0.26	0.03
	0.75–1	0.00	0.00	0.00	0.12	0.73	0.97
K.....	0–0.25	1.00	0.80	0.18	0.04	0.00	0.00
	0.25–0.5	0.00	0.20	0.48	0.25	0.09	0.00
	0.5–0.75	0.00	0.00	0.31	0.44	0.28	0.01
	0.75–1	0.00	0.00	0.03	0.26	0.63	0.99
L.....	0–0.25	1.00	0.86	0.14	0.02	0.00	0.00
	0.25–0.5	0.00	0.14	0.59	0.24	0.05	0.00
	0.5–0.75	0.00	0.00	0.18	0.47	0.36	0.05
	0.75–1	0.00	0.00	0.08	0.27	0.58	0.95
P.....	0–0.25	0.94	0.74	0.26	0.04	0.00	0.00
	0.25–0.5	0.05	0.25	0.50	0.27	0.01	0.00
	0.5–0.75	0.01	0.01	0.24	0.55	0.24	0.01
	0.75–1	0.00	0.00	0.00	0.14	0.74	0.99
Q.....	0–0.25	0.96	0.55	0.33	0.14	0.01	0.00
	0.25–0.5	0.04	0.32	0.36	0.27	0.08	0.00
	0.5–0.75	0.00	0.13	0.27	0.38	0.25	0.01
	0.75–1	0.00	0.00	0.04	0.21	0.66	0.99
R.....	0–0.25	1.00	0.66	0.21	0.12	0.03	0.00
	0.25–0.5	0.00	0.26	0.36	0.23	0.16	0.00
	0.5–0.75	0.00	0.08	0.32	0.36	0.26	0.05
	0.75–1	0.00	0.00	0.11	0.30	0.55	0.95
S.....	0–0.25	0.98	0.57	0.30	0.12	0.02	0.00
	0.25–0.5	0.02	0.29	0.30	0.28	0.14	0.00
	0.5–0.75	0.00	0.13	0.27	0.33	0.27	0.04
	0.75–1	0.00	0.01	0.13	0.26	0.58	0.96
T.....	0–0.25	0.98	0.60	0.24	0.11	0.06	0.01
	0.25–0.5	0.02	0.25	0.31	0.25	0.19	0.00
	0.5–0.75	0.00	0.13	0.25	0.31	0.32	0.03
	0.75–1	0.00	0.03	0.20	0.32	0.42	0.96

have identical initial and final mass fractions (i.e., $m_i/M_i = m/M$), so that the merger remnant's helium profile would be the same as in the parent stars. In the equal-mass cases A, B, C, J, K, and L, we do find $\langle m_i/M_i \rangle \approx m/M$ and the final helium profiles are indeed quite similar to the parent profile, as shown in § 4.3.

Along with equation (20), the functions of Figures 15 and 16 provide the means for approximating the final profile of any passively advected quantity. As a concrete example of how to use this method, we will now calculate the fractional helium abundance at $m/M = 0.28$ in the merger remnant of case G, using the same initial profiles as shown in Figure 2. From the solid lines corresponding to case G in Figures 15*c* and 16, we find that $\langle m_1/M_1 \rangle|_{0.28} = 0.05$, $\langle m_2/M_2 \rangle|_{0.28} = 0.65$ and $p_1(0.28) = 0.62$. Therefore,

$$Y(0.28) \approx 0.62 \times Y_1(0.05) + (1 - 0.62) \times Y_2(0.65) = 0.70 , \quad (21)$$

where we have used $Y_1(0.05) = 0.97$ and $Y_2(0.65) = 0.25$, obtained from the solid and short-dashed lines of Figure 2, respectively. By repeating this calculation for other values of m/M, we construct the approximate helium profile shown as the dashed line in Figure 17. Also shown for comparison is the "exact" profile (*solid line*) constructed by considering the individual helium abundance carried by each particle (the same curve that appears in Fig. 11*b*). We consider the agreement to be quite good, given the simplicity of the approximation scheme and the fact that it does not require access to large data files containing information on all $N = 3 \times 10^4$ particles.

4.5. *Degree of Spurious Mixing*

In all SPH calculations, numerical noise can lead to spurious, or artificial, mixing of SPH particles. To estimate how much of the observed mixing is in fact spurious, we have performed a series of systematic tests to evaluate quantitatively the effects of spurious transport in SPH calculations (Lombardi et al. 1996). In particular, one of these tests measures, in the absence of shocks and as a function of the neighbor number N_N and local noise level $v_{\rm rms}$ (the root mean square particle velocity deviation from the local

1996ApJ...468..797L

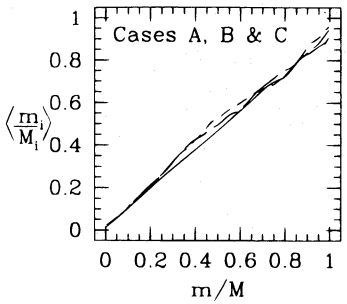

FIG. 15a

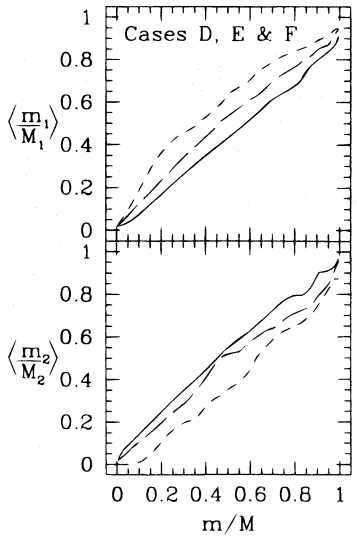

FIG. 15b

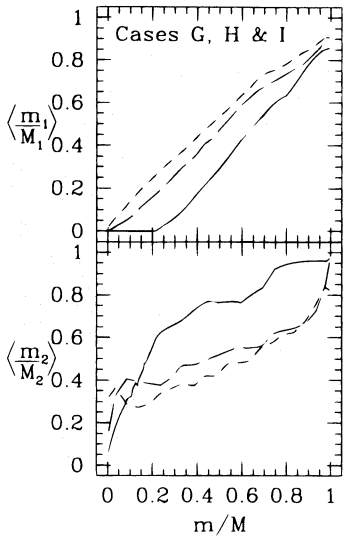

FIG. 15c

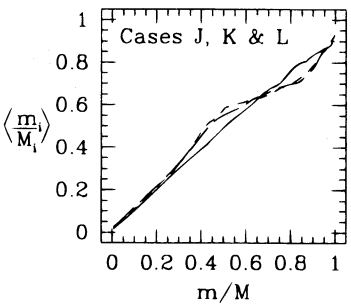

FIG. 15d

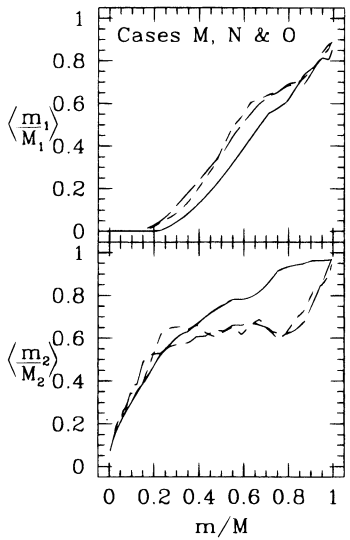

FIG. 15e

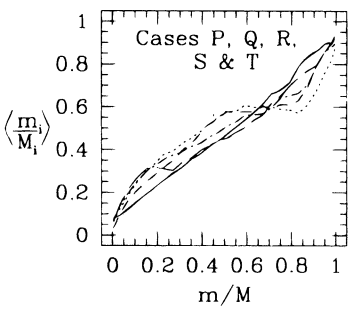

FIG. 15f

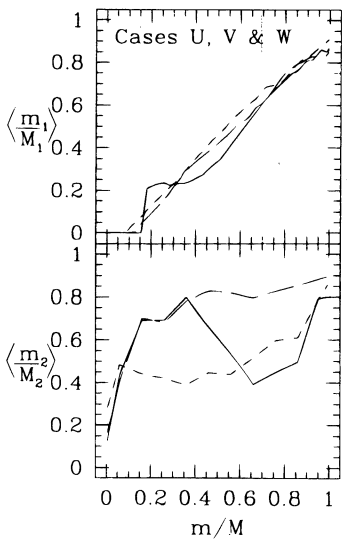

FIG. 15g

FIG. 15.—Average initial mass fractions $\langle m_i/M_i \rangle$ as a function of final mass fraction m/M for the following cases: (*a*) A, B, and C; (*b*) D, E, and F; (*c*) G, H, and I; (*d*) J, K, and L; (*e*) M, N, and O; (*f*) P, Q, R, S, and T; and (*g*) U, V, and W. As in Fig. 13, the different lines correspond to different pericenter separations r_p for the initial orbit. For collisions involving two identical parent stars, $\langle m_1/M_1 \rangle = \langle m_2/M_2 \rangle$, so that only one set of plots is necessary.

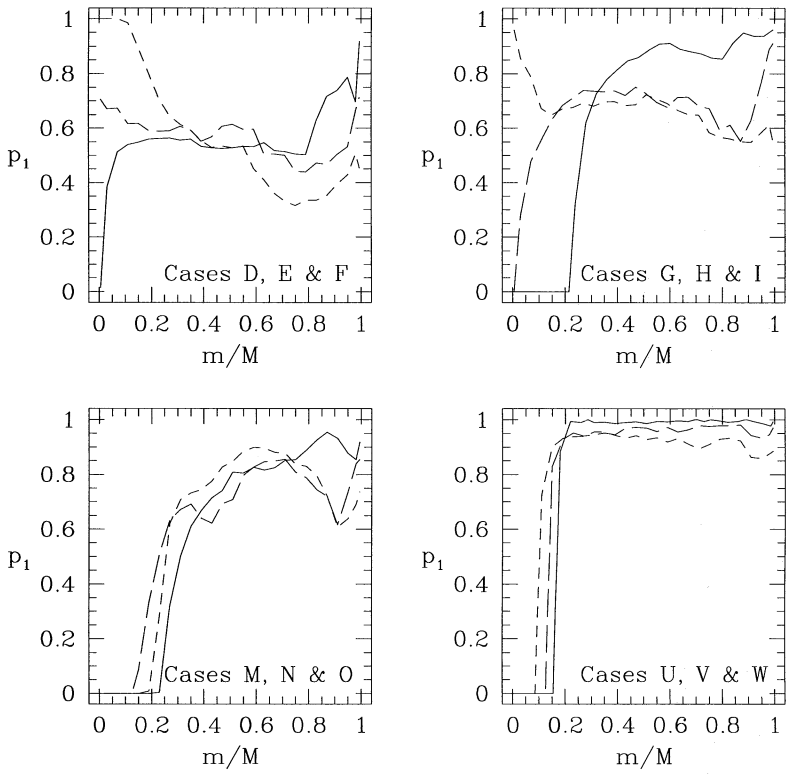

FIG. 16.—Probability p_1 that a particle in the merger remnant originated in star 1, as a function of final mass fraction m/M for the following cases: (*a*) D, E, and F; (*b*) G, H, and I; (*c*) M, N, and O; and (*d*) U, V, and W. The solid, long-dashed, and short-dashed lines correspond to collisions with pericenter separation $r_p = 0$, 0.25, and $0.5(R_1 + R_2)$, respectively. Collisions involving stars of equal mass necessarily have $p_1 = \frac{1}{2}$, and therefore p_1 is not displayed for such cases.

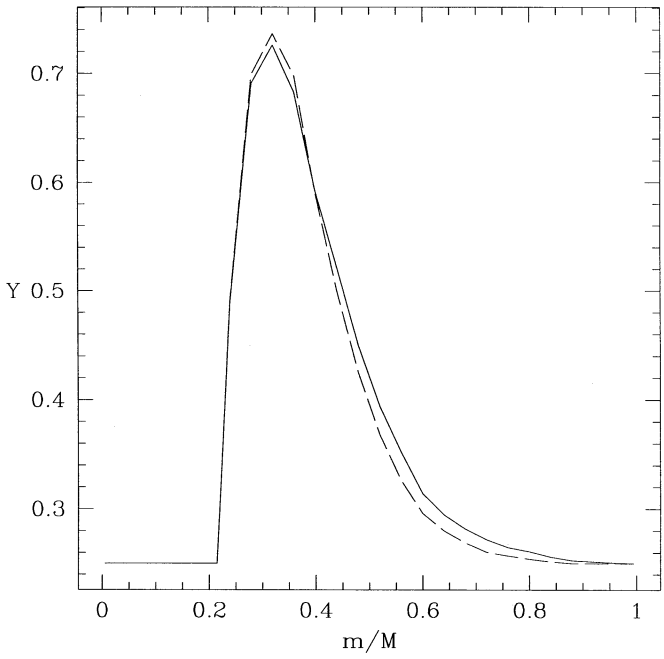

FIG. 17.—Exact (*solid line*) and approximate (*dashed line*) helium abundance profiles for the final merger remnant of case G. The exact profile was calculated using the values of Y_i (for all $N = 3 \times 10^4$ particles) derived from our assumed initial composition profiles. The approximate profile was derived by using eq. (20) and the curves of Figs. 15 and 16 corresponding to case G.

mean), dimensionless spurious diffusion coefficients defined by

$$D \equiv \left\langle \frac{n^{1/3}}{c_s} \frac{d\,\Delta r_s^2}{dt} \right\rangle , \tag{22}$$

where the angle brackets denote a time average, $\Delta r_s = (\Delta x_s^2 + \Delta y_s^2 + \Delta z_s^2)^{1/2}$ is the total distance traveled by a particle due to spurious diffusion, n is the local number density of SPH particles, c_s is the local sound speed and t is time.

Although strong shocks in SPH calculations can lead to direct particle penetration (Monaghan 1989), the parabolic calculations considered here typically lead to rather weak shocks and we believe particle diffusion dominates any spurious mixing. Once measured, the diffusion coefficients can be applied to give an estimate for the spurious deviation in a particle's position: after monitoring its local values of $v_{\rm rms}$, n, and c_s as a function of time t, this spurious deviation is estimated by numerically integrating

$$\Delta r_s^2 \approx \int D \frac{n^{-1/3}}{c_s}\, dt . \tag{23}$$

From the local density gradient $\nabla\rho$ at the particle's final position we can then approximate the error in its final mass fraction according to

$$\Delta m_s \approx 3^{-1/2} \Delta r_s |\nabla\rho| , \tag{24}$$

where the $3^{-1/2}$ arises from assuming isotropic spurious transport and accounts for the interior mass fraction being changed only by motion normal to surfaces of constant density. By repeating this procedure for all the particles, we arrive at an average spurious diffusion distance $\langle \Delta r_s \rangle$ and mass fraction $\langle |\Delta m_s| \rangle$, as well as a root mean square spurious displacement $\langle \Delta r_s^2 \rangle^{1/2}$ and mass fraction $\langle \Delta m_s^2 \rangle^{1/2}$. This method of estimating spurious diffusion distances will be referred to as Method I.

In the case of a head-on collision, a method that makes use of the axisymmetry around the collision axis (the x-axis), Method II, can also be applied. Assuming that the system remains axisymmetric throughout the entire dynamical evolution (this would not be the case if, e.g., Rayleigh-Taylor instabilities were to develop), then a particle should always remain in the plane defined by the collision axis and the particle's initial position. The distance to which a particle moves in the direction perpendicular to this plane immediately provides an estimate of the spurious displacement, simply by multiplying by $3^{1/2}$ (again we approximate the spurious motion as locally isotropic). We finally convert the spurious diffusion distance to an error in mass fraction exactly as in Method I (see eq. [24]). The advantage of Method II is that it does not approximate spurious transport as being a diffusive process, but instead exploits the special geometry of a head-on collision to directly account for spurious mixing, even in the presence of shocks.

The results of the two methods applied to our calculations are given in Table 5. When two numbers are given, the second one has been calculated by Method II. Included in this table are the average spurious diffusion distance $\langle \Delta r_s \rangle$, the root mean square diffusion distance $\langle \Delta r_s^2 \rangle^{1/2}$, the average equivalent mass fraction $\langle |\Delta m_s| \rangle / M$, and the root mean square mass fraction $\langle \Delta m_s^2 \rangle^{1/2} / M$. It is clear that the two methods are generally in good agreement, and that, when expressed in terms of m/M, the effects of spurious diffusion are always small.

A particle with a given initial interior mass fraction m_i/M_i has some preferred final mass fraction m/M, as discussed in § 4.4 and as can be seen from the clustering of points in Figure 14. Let $\Delta m_o/M$ be the difference between this preferred final mass fraction and the observed final mass fraction for a particular particle. Averaging over all particles, the quantities $\langle |\Delta m_o| \rangle / M$ and $\langle \Delta m_o^2 \rangle^{1/2} / M$, listed in Table 5, then quantify the observed degree of mixing (including both physical and spurious mixing) during the collision. The last column of Table 5 then subtracts the contribution $\langle \Delta m_s^2 \rangle$ due to spurious mixing from the total square deviation $\langle \Delta m_o^2 \rangle$, giving an estimate for the degree of mixing expected in a hypothetical simulation free of numerical errors. For example, in case G, we observe a root mean square spread in the interior mass fraction of $\langle \Delta m_o^2 \rangle^{1/2} / M = 0.09$. Using Method I, we estimate that the root mean square spread in interior mass fraction due to spurious mixing is $\langle \Delta m_s^2 \rangle^{1/2} / M \approx 0.036$, while Method II gives an estimate of 0.057 for this quantity. We therefore believe that the physical root mean square spread (i.e., the spread in a calculation free of spurious diffusion) would be approximately 0.08 or 0.07, depending on whether Method I or Method II is more accurate.

5. SUMMARY AND DISCUSSION

The main results of this paper can be summarized as follows. The typical merger remnants produced by collisions are rapidly and differentially rotating, and are far from chemically homogeneous, with composition profiles that can be rather peculiar in certain cases. For example, it often happens that the maximum helium abundance does not occur at the center of the remnant (see Fig. 11*b*). The merger remnants produced by our dynamical calculations, although very close to hydrostatic equilibrium, are usually far from thermal equilibrium. In particular, the remnants are not barotropes, i.e., the condition $d\Omega/dz = 0$ is generally not satisfied), and their temperature profiles can have positive gradients ($dT/dr > 0$) in certain regions.

At a qualitative level, many of our results can be understood very simply in terms of the requirement of convective stability in the final merger remnant. If entropy production

TABLE 5

ESTIMATES OF SPURIOUS DIFFUSION DISTANCES AND MASS FRACTIONS

Case	$\langle \Delta r_s \rangle$	$\langle \Delta r_s^2 \rangle^{1/2}$	$\langle \lvert\Delta m_s\rvert \rangle / M$	$\langle \Delta m_s^2 \rangle^{1/2} / M$	$\langle \lvert\Delta m_o\rvert \rangle / M$	$\langle \Delta m_o^2 \rangle^{1/2} / M$	$(\langle \Delta m_o^2 \rangle - \langle \Delta m_s^2 \rangle)^{1/2} / M$
A	0.19 0.13	0.45 0.42	0.027 0.029	0.036 0.042	0.07	0.09	0.08 0.07
B	0.31	0.66	0.037	0.045	0.08	0.11	0.10
C	0.33	0.86	0.040	0.050	0.09	0.11	0.10
D	0.17 0.11	0.37 0.30	0.032 0.029	0.043 0.041	0.07	0.09	0.08 0.08
E	0.26	0.58	0.037	0.045	0.09	0.12	0.11
F	0.30	0.64	0.041	0.053	0.09	0.12	0.11
G	0.16 0.12	0.42 0.36	0.028 0.039	0.036 0.057	0.07	0.09	0.08 0.07
H	0.22	0.52	0.038	0.050	0.13	0.18	0.18
I	0.27	0.63	0.044	0.059	0.12	0.17	0.15
J	0.18 0.12	0.38 0.32	0.034 0.029	0.047 0.042	0.07	0.09	0.08 0.08
K	0.24	0.53	0.038	0.046	0.11	0.14	0.14
L	0.34	0.93	0.042	0.053	0.11	0.14	0.13
M.....	0.17 0.11	0.37 0.27	0.039 0.041	0.054 0.060	0.08	0.10	0.08 0.08
N	0.21	0.51	0.037	0.045	0.12	0.17	0.16
O	0.24	0.59	0.038	0.046	0.13	0.17	0.16
P	0.32 0.29	0.66 0.77	0.032 0.041	0.041 0.057	0.11	0.13	0.13 0.12
Q	0.37	0.81	0.038	0.045	0.16	0.20	0.19
R	0.43	0.84	0.051	0.078	0.17	0.20	0.19
S.....	0.42	0.84	0.041	0.055	0.18	0.22	0.21
T	0.46	1.21	0.039	0.051	0.20	0.24	0.23
U	0.15 0.10	0.36 0.32	0.055 0.050	0.084 0.094	0.09	0.13	0.10 0.09
V	0.20	0.50	0.050	0.078	0.09	0.13	0.10
W.....	0.25	0.64	0.054	0.087	0.11	0.16	0.13

in shocks could be neglected (which may be reasonable for parabolic collisions, especially in the head-on case), then one could predict the remnant's composition profile simply by observing the composition and entropy profiles of the parent stars. Convective stability requires that the specific entropy s increase from the center to the surface ($ds/dr > 0$) in the final hydrostatic equilibrium configuration. In the absence of shock heating, fluid elements would conserve their entropy, and the final composition profile of a merger remnant could therefore be determined simply by combining mass shells in order of increasing entropy, from the center to the outside. Many of our results follow directly. For example, in the case of a collision between two identical stars, the composition profile of the merger remnant must match that of the parent stars, since there is a one-to-one correspondence between entropy and chemical composition. For two stars of very different masses, the much lower entropy material of the lower mass star tends to concentrate at the center of the final configuration, leading to the unusual composition and temperature profiles seen in Figures 13*c*, 13*e*, and 13*g*.

Regions where the dynamical stability criterion $ds/dr > 0$ (eq. [18]) is satisfied can nevertheless be thermally, or secularly, unstable. The small vertical oscillations [at the local Brunt-Väisälä frequency $\Omega_{BV} \propto (ds/dr)^{1/2}$] of a fluid element in such a region have amplitudes that grow slowly, and mixing will occur on a timescale comparable to the local radiative damping time (see, e.g., Kippenhahn & Weigert, chap. 6). The thermal instability can be of two types. When $d\mu/dr > 0$ and $dT/dr > 0$ (as in Figs. 13*c*, 13*e*, and 13*g*), a so-called thermohaline instability can develop, allowing fingers of the high-μ material to penetrate down into the lower μ, colder material below (see, e.g., Ulrich 1972). When such mixing occurs in the stellar core, it tends to increase the central helium abundance and therefore decrease the time that the merger remnant can remain on the MS.

When $d\mu/dr < 0$ but $dT/dr < (dT/dr)_{ad}$, so-called semiconvection can occur (Spruit 1992). In terms of easily computed SPH variables, the criterion for semiconvection is

$$0 < \frac{1}{A}\frac{dA}{dr} < -\frac{\Gamma_1}{\mu}\frac{d\mu}{dr}, \qquad (25)$$

where A is related to specific entropy by equation (4). We have tested our merger remnants formed from head-on collisions (which are spherically symmetric in structure) and found this instability typically to be present. Since the chemical composition of the remnant is never spherically symmetric, equation (25) must be checked along many different radial vectors. Figure 18 shows, as a function of the final mass fraction m/M, the fraction f_{sc} of gas that is semiconvective for six of our merger remnants. In all cases no semiconvective instability exists in the outer $\sim$20% of the mass, so that we do not expect this mixing mechanism can increase the helium abundance of the outer layers. Figure 18 does demonstrate, however, that some merger remnants (those of cases A, D, and J) have an unstable region that extends to the center, and these remnants therefore have a means of mixing hydrogen into their cores. For instance in case A, we see that the inner $\sim$40% could be significantly affected. In addition, the right-hand side of equation (25) changes as the fluid mixes, so that the details of this complicated process can only be followed numerically with a stellar evolution code.

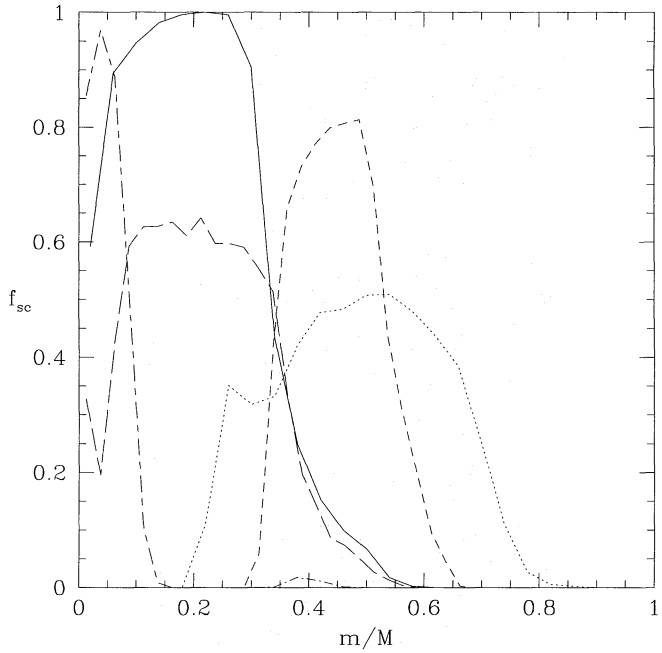

FIG. 18.—The fraction f_{sc} of gas unstable to semiconvection as a function of the mass fraction m/M in the merger remnants of the head-on cases A (*solid line*), D (*long-dashed line*), G (*short-dashed line*), J (*short- and long-dashed line*), M (*dotted and short-dashed line*), and U (*dotted line*).

For a rotating, chemically homogeneous star, stable thermal equilibrium requires $d\Omega/dz = 0$, where Ω is the angular velocity and z is measured parallel to the rotation axis (the Goldreich-Schubert stability criterion; see, e.g., Tassoul 1978, chap. 7). From the representative set of specific angular momentum contours presented in Figure 12, it is therefore evident that the merger remnants of cases Q, R, S, and T (which are chemically homogeneous, since their parent stars were fully mixed) cannot be in thermal equilibrium. In chemically inhomogeneous stars, regions with a sufficiently large and stabilizing composition gradient ($d\mu/dr < 0$) can in principle still be thermally stable even with $d\Omega/dz \neq 0$. However, it seems unlikely that the composition profiles generated dynamically by a collision would conspire to keep the remnants everywhere thermally stable.

The angular momentum distribution in a star can have significant effects on its characteristics (e.g., Deupree 1990). For instance, a star with a rapidly rotating core can have its MS lifetime extended beyond that of its nonrotating counterpart (e.g., Clement 1994). The fact that much of the angular momentum is hidden deep in the remnant's interior suggests a possible explanation for why observations of blue stragglers in open clusters such as M67 find no signs of rapid rotation (Peterson, Carney, & Latham 1984; Mathys 1987). Recently, Leonard & Livio (1995) have argued that the spin-down timescale of blue stragglers due to magnetic breaking is only $\sim 10^5$ yr, so that initially rapidly rotating merger remnants may not be a problem for the collisional formation scenario.

Stellar encounters with pericenter separations r_p larger than those considered in this paper are difficult to compute directly with SPH, since the amount of orbital energy ΔE dissipated during the first interaction is then so small that the integration time until the next pericenter passage can be several orders of magnitude larger than the hydrodynamic

time. We believe that our results can be safely extrapolated all the way to values of $r_p \approx 1.2(R_1 + R_2)$. For instance, from our results for collisions of equal-mass stars, it seems very likely that the helium profile of the merger remnant will always mimic that of the parent stars. In Figure 13*f*, note that the density, entropy, and temperature profiles also seem to be converging onto a fixed profile, and that the profiles for the $r_p = 0.5$, 0.75, and $0.95(R_1 + R_2)$ cases all look very similar. For $r_p \gtrsim 1.2(R_1 + R_2)$ the encounter is better described as a tidal capture than a collision, i.e., the amount of energy dissipated is sufficient to form a bound system, but no direct collision occurs, even in the outer layers of the stars. The maximum value $r_p = r_{\rm cap}$ for tidal capture can be calculated accurately from linear perturbation theory (Press & Teukolsky 1977; McMillan, McDermott, & Taam 1987). For two identical 0.8 $M_\odot$ MS stars and a relative velocity at infinity $v_\infty = 10$ km s^{-1}, McMillan et al. (1987) find $r_{\rm cap}/(R_1 + R_2) \approx 1.4$, which leaves little room for "clean" tidal captures. In addition, the long-term evolution of a tidal-capture binary may well lead to merging of the two stars even if the initial interaction is in the linear regime (for recent discussions, see Mardling 1995a, 1995b, and Kumar & Goodman 1996).

It must be stressed that the amount of mixing determined by SPH calculations is always an upper limit. Indeed, some of the mixing observed in a calculation will always be a numerical artifact. Low-resolution SPH calculations in particular tend to be very noisy, and the noise can lead to spurious mixing of SPH particles, independent of any real physical mixing of fluid elements. The degree of spurious mixing in our calculations is evaluated by two simple, approximate methods in § 4.5. The diffusion coefficients used in Method I have been measured in the absence of shocks and artificial viscosity, effects that could alter the degree of spurious mixing. Method II works only for head-on collisions and assumes that we can safely neglect any nonaxisymmetric instabilities. Furthermore, both methods assume that spurious transport is isotropic, which may not be true in the presence of strong entropy gradients. Despite these simplifying assumptions, the reasonable agreement between the two methods (see Table 5) gives us confidence that they do yield correct order-of-magnitude error estimates of spurious mixing. The results demonstrate that spurious mixing does not significantly corrupt our simulations, as can be seen by the near agreement of numbers in the last two columns of Table 5. The general question of spurious transport in SPH calculations will be addressed in a separate paper (Lombardi et al. 1996).

BH performed the first fully three-dimensional calculations of colliding MS stars. In contrast to the present work, they considered only identical $n = 1.5$ polytropes, which are mostly relevant for collisions of low-mass stars ($M_1 = M_2 \lesssim 0.4\ M_\odot$). The results of their parabolic collisions agree qualitatively with our analogous calculations (cases P, Q, R, S, and T). The agreement is especially good for the innermost region of a merger remnant formed from a head-on collision (case P in this paper): the short total integration time and the locally high density together keep spurious mixing small in both BH and our calculations. Typically, BH finds a somewhat higher degree of mixing than we report in our Table 4. For instance, in our case P, 74% of the particles in the outer quarter (by mass) of the merger remnant began in the outer quarter of a parent star, while in BH's analogous collision only about 55% of the particles remain in the outer quarter. In our case T, a grazing collision, 60% of the particles that began in the inner quarter of a parent star ended in the inner quarter of the merger remnant, while that number is less than 50% in BH's analogous collision. Also note, again for case T, that only 3% of the fluid in the inner quarter of the remnant originated in the outer quarter of a parent star, as opposed to over 10% in BH. We have also simulated a number of collisions analogous to cases P, Q, R, S, and T, but with $N = 1024$ particles, as in BH, instead of $N = 3 \times 10^4$. We find levels of mixing consistent with BH and conclude that the differences in results between our $n = 1.5$ polytrope collisions and those of BH arise from a lower degree of spurious mixing in our calculations due to the larger particle number.

From the final column of Table 5, note that our collisions of $n = 1.5$ polytropes (cases P, Q, R, S, and T) generally exhibit a somewhat higher degree of mixing than observed in our other calculations, especially collisions involving two TAMS stars (cases A, B, and C). This is not surprising since parent stars of constant entropy, which are only marginally stable against convection, should be easier to mix than those with significant positive entropy gradients (stable stratifications). In addition, the more homogeneous density profile of $n = 1.5$ polytropes leads to a better distribution of the impact energy throughout the entire mass of fluid. Therefore, the generally lower degree of mixing in our results, as compared to BH, can be understood not only from the better resolution in our simulations, but also because the structure of our higher mass parent stars makes the fluid more difficult to mix.

Benz & Hills (1992) have performed calculations of collisions between $n = 1.5$ polytropes with a mass ratio $M_2/M_1 = 0.2$. Given the low masses of the MS stars involved ($M_1 \lesssim 0.4\ M_\odot$, hence $M_2 < 0.1\ M_\odot$), these calculations are not directly relevant to blue straggler formation. Since none of our simulations model such low masses, no direct comparison with our results is possible.

Our results could be improved upon or extended in a number of ways. For instance, although ideal gas pressure dominates, the equation of state could be extended to include radiation, partial ionization, and electron degeneracy corrections. More accurate initial composition profiles could also be implemented. Note, however, that our results can be applied to arbitrary initial profiles by the method of § 4.4. Incidentally, profiles of ^{7}Li would be particularly interesting to consider, since this element is destroyed at temperatures $T \gtrsim 10^6$ K and is therefore an observationally measurable indicator of mixing (see, e.g., Hobbs & Mathieu 1991 and Pritchet & Glaspey 1991). Our dynamical calculations and the determination of hydrodynamical mixing are only the first step in modeling blue straggler formation. The merger remnants, which are much larger than normal equilibrium MS stars of the same mass, will recontract to the MS on a thermal timescale ($\sim 10^6$ yr). As they evolve, mixing processes such as meridional circulation, semiconvection and convection may well be important. Calculations of this thermal relaxation phase using the results of dynamical calculations, such as those presented in this paper, as initial conditions will be necessary in order to make detailed predictions for the observable parameters of blue stragglers.

Recently, Sills, Bailyn, & Demarque (1995, hereafter SBD) have begun to investigate the consequences of blue

stragglers being born unmixed, i.e., with composition profiles matching those of their parents. To create an unmixed model of a nascent blue straggler formed by the collision of two TAMS stars, SBD relaxes a nonrotating TAMS star whose mass has been artificially doubled but which is otherwise unchanged. The subsequent stellar evolution is contrasted to that of a fully mixed (i.e., chemically homogeneous) blue straggler. SBD finds that the high central helium concentration in the unmixed models causes the time spent on the MS ($\sim 5 \times 10^7$ yr) to be drastically shorter than for the fully mixed counterparts ($\sim 5 \times 10^8$ yr), making it difficult to account for the number of observed blue stragglers in the core of NGC 6397. In addition, the color and brightness of such unmixed blue stragglers do not match these observations. A blue straggler population composed solely of nonrotating, unmixed merger remnants of two TAMS parent stars is therefore not sufficient to explain the core blue stragglers in NGC 6397. On the other hand, preliminary results of a study by Ouellette & Pritchet (1996) for about 300 blue stragglers in 16 different clusters suggest that unmixed initial models may better explain the observed properties of some blue stragglers.

Additional work following the approach of SBD and Ouellette & Pritchet (1996) would clearly be beneficial. A number of factors need to be considered in more detail. For instance, the profiles of Figure 13 can be used to specify the structure of a (zero-age) blue straggler and thereby improve upon the initial models adopted in SBD. In addition, it is unrealistic to expect that all collisional blue stragglers are born only from head-on collisions of TAMS parent stars: most blue stragglers will be formed from off-axis collisions and will consequently be born rapidly rotating, especially in their cores, which affects their observable characteristics and extends their lifetime on the MS (e.g., Deupree 1990; Clement 1994). Attention must also be given to collisions between unequal-mass parent stars, which form merger remnants with profiles that are neither homogeneous nor like that of the parents (i.e., such remnants are neither fully mixed nor unmixed). Since these blue stragglers have a greatly enhanced (and even possibly primordial) hydrogen abundance in their cores, they are excellent blue straggler candidates: they are expected to remain on the MS for a much longer time than their unmixed counterparts considered by SBD.

We thank Charles Bailyn, Alison Sills, and the anonymous referee for useful comments. Support for this work was provided by NSF grant AST 91-19475, NASA grant NAG 5-2809, NASA grant HF-1037.01-92A, and the Alfred P. Sloan Foundation. Computations were performed at the Cornell Theory Center, which receives major funding from the NSF and IBM Corporation, with additional support from the New York State Science and Technology Foundation and members of the Corporate Research Institute.

REFERENCES

Bacon, R., Sigurdsson, S., & Davies, M. B. 1996, MNRAS, in press
Bailyn, C. D. 1992, ApJ, 392, 519
———. 1995, ARA&A, 33, 133
Bailyn, C. D., & Pinsonneault, M. H. 1995, ApJ, 439, 705
Benz, W., & Hills, J. G. 1987, ApJ, 323, 614 (BH)
———. 1992, ApJ, 389, 546
Chandrasekhar, S. 1939, An Introduction to the Theory of Stellar Structure (Chicago: Univ. Chicago Press)
———. 1969, Ellipsoidal Figures of Equilibrium (New Haven: Yale Univ. Press)
Clayton, D. D. 1983, Principles of Stellar Evolution and Nucleosynthesis (Chicago: Univ. Chicago Press)
Clement, M. J. 1994, ApJ, 420, 797
Côté, P., Welch, D. L., Fischer, P., Da Costa, G. S., Tamblyn, P., Seitzer, P., & Irwin, M. J. 1994, ApJS, 90, 83
D'Antona, F. 1987, ApJ, 320, 653
Davies, M. B., & Benz, W. 1995, MNRAS, 276, 876
De Marchi, G., & Paresce, F. 1994, ApJ, 422, 597
Deupree, R. G. 1990, ApJ, 357, 175
Hernquist, L. 1993, ApJ, 404, 717
Hernquist, L., & Katz, N. 1989, ApJS, 70 419
Hills, J. G., & Day, C. A. 1976, Astrophys. Lett., 17, 87
Hobbs, L. M., & Mathieu, R. D. 1991, PASP, 103, 431
Hockney, R. W., & Eastwood, J. W. 1988, Computer Simulations Using Particles (Bristol: Adam Hilger)
Hut, P., et al. 1992, PASP, 104, 981
Jahn, K., Kałużny, J., & Ruciński, S. M. 1995, A&A, 295, 101
Kałużny, J., & Ruciński, S. M. 1993, in ASP Conf. Ser. 53, Blue Stragglers, ed. R. A. Saffer (San Francisco: ASP), 164
Kippenhahn, R., & Weigert, A. 1990, Stellar Structure and Evolution (Berlin: Springer)
Kumar, P., & Goodman, J. 1996, ApJ, 466, in press
Lai, D., Rasio, F. A., & Shapiro, S. L. 1993, ApJ, 412, 593
———. 1994, ApJ, 423, 344
Landau, L. D., & Lifshitz, E. M. 1959, Fluid Mechanics (New York: Pergamon Press)
Leonard, P. J. T. 1989, AJ, 98, 217
Leonard, P. J. T., & Fahlman, G. G. 1991, AJ, 102, 994
Leonard, P. J. T., & Livio, M. 1995, ApJ, 447, L121
Livio, M. 1993, in ASP Conf. Ser., 53, Blue Stragglers, ed. R. A. Saffer (San Francisco: ASP), 3
Lombardi, J. C., Jr., Rasio, F. A., & Shapiro, S. L. 1995, ApJ, 445, L117
———. 1996, in preparation
Mardling, R. A. 1995a, ApJ, 450, 722
———. 1995b, ApJ, 450, 732
Mateo, M., Harris, H. C., Nemec, J., & Olszewski, E. W. 1990, AJ, 100, 469
Mathys, G. 1987, A&A, 245, 467
McMillan, S. L. W., McDermott, P. N., & Taam, R. E. 1987, ApJ, 318, 261
Milone, A. A. E., & Latham, D. W. 1994, AJ, 108, 1828
Monaghan, J. J. 1985, Comp. Phys. Rep., 3, 71
———. 1989, J. Comp. Phys., 82, 1
———. 1992, ARA&A, 30, 543
Monaghan, J. J., & Lattanzio, J. C. 1985, A&A, 149, 135
Ouellette, J., & Pritchet, C. 1996, in ASP Conf. Ser. 90, Binaries in Clusters, ed. E. Milone & J.-C. Mermilliod (San Francisco: ASP), 356
Peterson, R. C., Carney, B. W., & Latham, D. W. 1984, ApJ, 279, 237
Press, W. H., & Teukolsky, S. A. 1977, ApJ, 213, 183
Pritchet, C. J., & Glaspey, J. W. 1991, ApJ, 373, 105
Rappaport, S., Verbunt, F., & Joss, P. C. 1983, ApJ, 275, 713
Rasio, F. A. 1991, Ph.D. thesis, Cornell Univ.
———. 1995, ApJ, 444, L41
Rasio, F. A., & Shapiro, S. L. 1995, ApJ, 438, 887
Ruciński, S. M. 1988, AJ, 95, 1895
Shapiro, S. L., & Teukolsky, S. A. 1983, Black Holes, White Dwarfs, and Neutron Stars (New York: Wiley)
Shara, M. M., Drissen, L., Bergeron, L. E., & Paresce, F. 1995, ApJ, 441, 617
Sienkiewicz, R., Bahcall, J. N., & Paczyński, B. 1990, ApJ, 349, 641
Sigurdsson, S., Davies, M. B., & Bolte, M. 1994, ApJ, 431, L115
Sigurdsson, S., & Phinney, E. S. 1995, ApJS, 99, 609
Sills, A. P., Bailyn, C. D., & Demarque, P. 1995, ApJ, 455, L163 (SBD)
Spitzer, L. 1987, Dynamical Evolution of Globular Clusters (Princeton: Princeton Univ. Press)
Spruit, H. C. 1992, A&A, 253, 131
Stryker, L. L. 1993, PASP, 105, 1081
Tassoul, J. 1978, Theory of Rotating Stars (Princeton: Princeton Univ. Press)
Ulrich, R. K. 1972, ApJ, 172, 165
Wells, N. H., Burrus, C. S., Desorby, G. E., & Boyer, A. L. 1990, J. Comp. Phys., 4, 507
Yan, L., & Mateo, M. 1994, AJ, 108, 1810
Yanny, B., Guhathakurta, P., Bahcall, J. N., & Schneider, D. P. 1994a, ApJ, 107, 1745
Yanny, B., Guhathakurta, P., Schneider, D. P., & Bahcall, J. N. 1994b, ApJ, 435, L59